

# Spatially resolving the volatile sulfur abundance in the HD 100546 protoplanetary disc

Luke Keyte<sup>1,2</sup>  Mihkel Kama,<sup>1,2</sup> Ko-Ju Chuang<sup>3</sup>  L. Ilsedore Cleeves,<sup>4</sup> Maria N. Drozdovskaya<sup>5</sup>  Kenji Furuya,<sup>6</sup> Jonathan Rawlings<sup>1</sup>  and Oliver Shorttle<sup>7</sup> 

<sup>1</sup>Department of Physics and Astronomy, University College London, Gower Street, WC1E 6BT London, United Kingdom

<sup>2</sup>Tartu Observatory, Observatoriumi 1, Tõrvavere 61602, Tartu, Estonia

<sup>3</sup>Laboratory for Astrophysics, Leiden Observatory, Leiden University, P.O. Box 9513, NL-2300 RA Leiden, the Netherlands

<sup>4</sup>Department of Astronomy, University of Virginia, Charlottesville, VA 22904, USA

<sup>5</sup>Center for Space and Habitability, Universität Bern, Gesellschaftsstrasse 6, CH-3012 Bern, Switzerland

<sup>6</sup>National Astronomical Observatory of Japan, Osawa 2-21-1, Mitaka, Tokyo 181-8588, Japan

<sup>7</sup>Department of Earth Sciences & Institute of Astronomy, University of Cambridge, CB3 OHA, United Kingdom

Accepted 2023 December 20. Received 2023 December 8; in original form 2023 October 13

## ABSTRACT

Volatile elements play a crucial role in the formation of planetary systems. Their abundance and distribution in protoplanetary discs provide vital insights into the connection between formation processes and the atmospheric composition of individual planets. Sulfur, being one of the most abundant elements in planet-forming environments, is of great significance, and now observable in exoplanets with *JWST*. However, planetary formation models currently lack vital knowledge regarding sulfur chemistry in protoplanetary discs. Developing a deeper understanding of the major volatile sulfur carriers in discs is essential to building models that can meaningfully predict planetary atmospheric composition, and reconstruct planetary formation pathways. In this work, we combine archival observations with new data from the Atacama Large sub-Millimeter Array (ALMA) and the Atacama Pathfinder EXperiment (APEX), covering a range of sulfur-bearing species/isotopologs. We interpret this data using the DALI thermo-chemical code, for which our model is highly refined and disc-specific. We find that volatile sulfur is heavily depleted from the cosmic value by a factor of  $\sim 1000$ , with a disc-averaged abundance of  $S/H \sim 10^{-8}$ . We show that the gas-phase sulfur abundance varies radially by  $\gtrsim 3$  orders of magnitude, with the highest abundances inside the inner dust ring and coincident with the outer dust ring at  $r \sim 150\text{--}230$  au. Extracting chemical abundances from our models, we find OCS, H<sub>2</sub>CS, and CS to be the dominant molecular carriers in the gas phase. We also infer the presence of a substantial OCS ice reservoir. We relate our results to the potential atmospheric composition of planets in HD 100546, and the wider exoplanet population.

**Key words:** planets and satellites: formation – protoplanetary discs – submillimetre: planetary systems.

## 1 INTRODUCTION

Sulfur is one of the most abundant elements in the Universe, essential to astrochemistry and biological processes. Understanding sulfur's path from the interstellar medium, through discs, and into planets is of increasing importance, relevant to the study of planetary formation and the search for life. Despite this, sulfur chemistry in star- and planet-forming environments is poorly understood. In the interstellar medium the total sulfur abundance is  $S/H = 1.32 \times 10^{-5}$ , of which 99 per cent is in the gas phase (Savage & Sembach 1996; Asplund et al. 2009). In molecular clouds, however, a factor of  $\geq 10$  depletion is observed (e.g. Tieftrunk et al. 1994). This missing sulfur constitutes one of the major outstanding questions in astrochemistry. Similarly, the main carrier of volatile sulfur in protoplanetary discs is also unknown. Chemical models predict the dominant volatile carriers to include species such as H<sub>2</sub>S, OCS, SO, SO<sub>2</sub>, and CS, but past

observations have typically lacked the sensitivity to definitively address the volatile sulfur budget in discs (e.g. Wakelam et al. 2004). In some systems, upper limits determined from non-detections have been used to provide useful constraints (e.g. Le Gal et al. 2021).

Some clues about sulfur's chemical pathway through molecular clouds and into planetary systems come from observations of our own Solar system, where sulfur-bearing species are routinely detected in comets. These are most often in the form of H<sub>2</sub>S and S<sub>2</sub> (Mumma & Charnley 2011), but also include a large variety of other species. Observations of 67P/Churyumov-Gerasimenko, for example, uncovered a wealth of sulfurated species in the cometary coma, including H<sub>2</sub>S, S, S<sub>2</sub>, S<sub>3</sub>, S<sub>4</sub>, SO, SO<sub>2</sub>, H<sub>2</sub>CS, CS<sub>2</sub>, OCS, C<sub>2</sub>H<sub>6</sub>S, CH<sub>3</sub>SH, and NH<sub>4</sub><sup>+</sup>SH<sup>-</sup> (Le Roy et al. 2015; Calmonte et al. 2016; Altweig et al. 2022). Such observations provide valuable insights into the conditions and processes that existed during the formation of the Solar system.

By comparison, observations of sulfur-bearing species in protoplanetary discs are relatively rare, with only six different molecules

\* E-mail: [luke.keyte.18@ucl.ac.uk](mailto:luke.keyte.18@ucl.ac.uk)

having been detected thus far; CS, SO, H<sub>2</sub>S, SO<sub>2</sub>, H<sub>2</sub>CS, and SiS (e.g. Dutrey et al. 2011; Guilloteau et al. 2013; Phuong et al. 2018; Le Gal et al. 2019; Booth et al. 2021; Law, Booth & Öberg 2023). Modelling of the sulfur budget in protoplanetary discs suggests that sulfur is highly depleted from the gas phase, but the split between rocky, icy, and gas-phase components is not well understood. Previous studies predict that the main refractory component is iron sulfide, FeS (Pasek et al. 2005), and that conversion from volatile molecules to FeS likely proceeds in the early stages of disc evolution when gas-phase molecules react with warm, iron-rich dust grains (Lazurkina, Kremser & Fegley 1996). Kama et al. (2019) inferred the refractory sulfur reservoir in a sample of discs around Herbig Ae/Be stars to be  $89 \pm 8$  per cent of the total sulfur, leaving  $11 \pm 8$  per cent distributed to volatile molecules. These stars have shallow surface convective zones, in which newly accreted material dominates the photospheric composition. Signatures of sulfur-bearing species in the photospheres of such stars are indicative of material passing through the inner cavity of the disc, and these systems therefore provide a unique laboratory for studying volatile sulfur budgets (Jermyn & Kama 2018).

In this work, we present observations from the ALMA 12m array and APEX telescope, covering nine transitions of eight sulfur-bearing species and their isotopologues in the protoplanetary disc HD 100546. We use the DALI 2D physical-chemical disc modelling code to constrain the abundance and spatial distribution of volatile sulfur-bearing species, and determine the total elemental gas-phase sulfur abundance. The aim is to gain a deeper understanding of the major volatile sulfur carriers in protoplanetary discs, and provide insights as to how their spatial distribution is linked to exoplanet bulk and atmospheric composition.

## 2 OBSERVATIONS

### 2.1 Target: HD 100546

HD 100546 is a well-studied  $2.49 \pm 0.02 M_{\odot}$  Herbig Be star of spectral type B9V, with an estimated age of  $\sim 5$  Myr (Arun et al. 2019), at a distance of  $110 \pm 1$  pc (Gaia Collaboration 2018). The star hosts a bright transition disc with an inclination of  $44^{\circ}$  and position angle of  $146^{\circ}$  (e.g. Walsh et al. 2014; Fedele et al. 2021), with a total observable dust mass of  $\sim 10^{-3} M_{\odot}$  (Wright et al. 2015; Miley et al. 2019). Micron-sized grains are observed out to at least 1000 au (Ardila et al. 2007). ALMA band 7 observations show that mm-sized grains are abundant out to  $\sim 230$  au, but are depleted inside of  $\sim 13$  au and again from 40 to 150 au (Walsh et al. 2014; Fedele et al. 2021). The inner cavity hosts a smaller inner disc extending from  $\sim 0.25$  to 1 au containing  $3 \times 10^{-10} M_{\odot}$  of dust (Benisty et al. 2010). Modelling suggests that the size of the inner cavity and outer gap are consistent with radial zones cleared of material by two planetary companions: a  $20M_{\oplus}$  planet at  $\sim 13$  au and a  $15M_{\oplus}$  planet at  $\sim 55$  au (Walsh et al. 2014; Currie et al. 2015; Pinilla, Birnstiel & Walsh 2015; Quanz et al. 2015). This interpretation is supported by infrared imaging with the Gemini Planet Imager, where point sources have been resolved at the same radial locations as the proposed planetary candidates (Currie et al. 2015). There is also evidence for a warped or misaligned inner gas disc, traced by deviations from Keplerian rotation in the CO  $J = 3-2$  emission. (Walsh et al. 2017; Booth et al. 2018).

CO isotopologue observations suggest that the molecular gas extends to at least  $\sim 390$  au (Walsh et al. 2014). A variety of atomic and molecular lines have been observed, including lines of atomic oxygen and atomic carbon (Thi et al. 2011; Kama et al. 2016a; Kama

et al. 2016b), spatially resolved CO 3–2 emission (Walsh et al. 2014), various CO isotopologues, and three H<sub>2</sub>O lines (Bruderer et al. 2012; Meeus et al. 2012, 2013; Kama et al. 2016b). Spatially resolved observations of SO with ALMA reveal emission from inside the dust cavity, likely related to thermal desorption of ices at the cavity wall (Booth et al. 2023b). This SO emission has also been linked to ongoing planet formation, thought to be tracing shocked gas in the vicinity of a circumplanetary disc. CS has also been detected, making HD 100546 one of only three discs where both SO and CS have been detected together, the others being HD 169142 (Law, Booth & Öberg 2023; Booth et al. 2023a) and AB Aur (Rivière-Marichalar et al. 2023). Azimuthal asymmetries observed in the emission morphology and spectral lines of each of these species have previously been used to infer an azimuthal C/O variation in the disc (Keyte et al. 2023). No other sulfur-bearing species have been detected in HD 100546 thus far. However, Kama et al. (2019) measured the total sulfur abundance in the stellar photosphere to be  $\log(S/H) = -5.37 \pm 0.5$ , thus providing an initial constraint on the volatile sulfur content of accreting material.

### 2.2 ALMA observations

We present ALMA observations of HD 100546 in band 3 from the cycle 5 programme 2017.1.00885.S (PI: M. Kama). Observations were completed in one execution block on 2017 October 24th, covering baseline lengths ranging from 41.4 to 13399.7 m. The total on-source time was 18.18 min. System temperatures varied from 45.4–81.3 K and the average precipitable water vapour was 0.7 mm. J0904–5735 was used as both the bandpass and flux calibrator, while J1145–6954 was used as the phase calibrator. The observations cover nine rotational transitions of eight sulfur-bearing species, outlined in Table 1.

The data reduction was completed using the ALMA Pipeline in the COMMON ASTRONOMY SOFTWARE PACKAGE (CASA) version 5.6.1-8 (McMullin et al. 2007). Self-calibration was performed but found to have marginal impact due to low signal-to-noise of the data. Continuum and line imaging were performed with the CLEAN algorithm using Briggs weighting (robust = 0.5). Continuum subtraction was performed with the CASA task *uvcontsub*, using a single-order polynomial fit to the line free channels. The spectral resolution and synthesized beam size for each of the transitions are listed in Table 1.

The inner dust ring was well-resolved in the continuum data, and the small inner dust disc ( $r \lesssim 1$  au) was detected. The continuum image is presented in Appendix A. No spectral lines were detected in any of the ALMA 12m array data. We initially attempted to extract the spectral lines from the CLEAN image cubes using an elliptical aperture with a  $3.9''$  radius centred on the source. Integrated intensity maps were created from the CLEAN cubes, which yielded no detections. We then employed a number of other techniques in order to increase the signal-to-noise ratio.

First, we stacked the lines in the image plane, by adding together the integrated intensity maps. This resulted in no detections. Next, we applied a Keplerian mask to each of the CLEAN image cubes in order to maximize the signal-to-noise in the image plane (Teague 2020). The Keplerian masked cubes were then used to create integrated emission maps, which again failed to result in any detections. Finally, we applied a matched filter to the visibility data, to maximize the signal-to-noise in the *uv*-plane (Loomis et al. 2018). The matched filter technique utilises a template image cube that samples the *uv*-space in order to obtain a set of template visibilities. These can then be used as a filter, which is cross-correlated with the data in an attempt

**Table 1.** Observational parameters for sulfur-bearing species in HD 100546 from ALMA and APEX data. Disc-integrated flux upper limits are at  $3\sigma$  level, denoted by ‘<’.

Molecule	Transition	$\nu$ (GHz)	$\Delta\nu$ (GHz)	Channels	$E_{\text{up}}$ (K) <sup>a</sup>	$A_{\text{ul}}$ ( $\text{s}^{-1}$ ) <sup>a</sup>	Beam size	Flux ( $\text{W/m}^2$ )
ALMA 12m array								
SiS	5–4	90.769	0.117	960	90.8	$1.19 \times 10^{-5}$	$0.10'' \times 0.07''$	$< 3.28 \times 10^{-19}$
$^{13}\text{C}^{34}\text{S}$	2–1	90.923	0.059	480	6.5	$1.34 \times 10^{-5}$	$0.10'' \times 0.07''$	$< 1.84 \times 10^{-19}$
$^{13}\text{CS}$	2–1	92.491	0.059	480	6.7	$1.41 \times 10^{-5}$	$0.10'' \times 0.07''$	$< 4.85 \times 10^{-20}$
$\text{SO}_2$	$3_{1,3}-2_{0,2}$	104.029	0.117	480	7.7	$1.01 \times 10^{-5}$	$0.09'' \times 0.06''$	$< 9.71 \times 10^{-20}$
$\text{SO}_2$	$10_{1,9}-10_{0,10}$	104.239	0.117	480	54.7	$1.12 \times 10^{-5}$	$0.09'' \times 0.06''$	$< 9.93 \times 10^{-20}$
$^{34}\text{SO}_2$	$10_{1,9}-10_{0,10}$	104.392	0.117	480	54.6	$1.10 \times 10^{-5}$	$0.09'' \times 0.06''$	$< 1.00 \times 10^{-18}$
$^{30}\text{SiS}$	6–5	105.059	0.117	480	17.7	$1.88 \times 10^{-5}$	$0.09'' \times 0.06''$	$< 1.88 \times 10^{-18}$
$\text{Si}^{34}\text{S}$	6–5	105.942	0.234	960	17.8	$1.90 \times 10^{-5}$	$0.09'' \times 0.06''$	$< 1.36 \times 10^{-19}$
APEX								
$\text{o-H}_2\text{S}$	$1_{1,0}-1_{0,1}$	168.763	0.090	160	27.9	$2.65 \times 10^{-5}$	$37.1'' \times 37.1''$	$< 1.06 \times 10^{-21}$

<sup>a</sup>Line frequencies, upper energy levels ( $E_{\text{up}}$ ), and Einstein A coefficients ( $A_{\text{ul}}$ ) are taken from the Cologne data base for molecular spectroscopy (Müller et al. 2001, 2005; Endres et al. 2016) and the Leiden atomic and molecular data base (Schöier et al. 2005).

to detect any weak emission. We created template emission profiles for each of the spectral windows in the ALMA 12m array data by modelling the spectral line emission with the DALI thermo-chemical disc modelling code (see Section 3). The matched filter was then run for each of the spectral lines individually, but again failed to result in any detections.

We derived  $3\sigma$  upper limits for the disc-integrated flux for each of the non-detected spectral lines, calculated from the elliptically masked integrated intensity maps (Table 1), where the mask extended  $3.9''$  [approximately covering the gas disc as traced by CO (Walsh et al. 2014)]. Spectra are presented in Fig. 1.

### 2.3 APEX observations

Observations of HD 100546 were carried out in band 5 ( $\sim 180$  GHz) with the single-pixel SEPIA receiver (Belitsky et al. 2018) on APEX, during several runs from 2021 March to 2021 September (programme 0108.F-9320, PI: L. Keyte). The observations targeted the  $\text{o-H}_2\text{S}$   $1_{1,0}-1_{0,1}$  transition at 168.762 GHz. The backend used was FFTS1, with a highest resolution channel space of 0.06 MHz or  $0.11 \text{ km s}^{-1}$ . Observational parameters are listed in Table 1.

A total of 209 scans were completed, with exposure times ranging from  $\sim 0.5$  to 7.5 min. Total observing time was 13.2 hr, with 143.1 min on-source. The column of precipitable water vapour was typically 2.5 mm, but ranged from 1.0 to 5.0 mm. Baseline subtraction and other high-level reductions were performed with GILDAS/CLASS (Pety 2018), and the data was smoothed to a velocity resolution of  $\delta\nu = 1 \text{ km s}^{-1}$ .

The  $\text{o-H}_2\text{S}$   $1_{1,0}-1_{0,1}$  transition at 168.76 GHz was not detected with APEX. At a spectral resolution of  $1 \text{ km s}^{-1}$ , the achieved rms is 1.53 mK, from which we derived a  $3\sigma$  upper limit on the disc-integrate flux of  $1.06 \times 10^{-21} \text{ W m}^{-2}$ . The spectrum is shown in Fig. 1.

### 2.4 Complementary data

We also make use of a variety of archival data. These include ALMA ACA observations of sulfur-bearing species first presented in Keyte et al. (2023; SO,  $^{34}\text{SO}$ ,  $\text{SO}_2$ , CS,  $\text{C}^{36}\text{S}$ ,  $\text{HCS}^+$ ,  $\text{H}_2\text{CS}$ ) and detections of SO  $7_{7}-6_{6}$  (301.286 GHz) and  $7_{8}-6_{7}$  (304.078 GHz) first presented in Booth et al. (2023b).

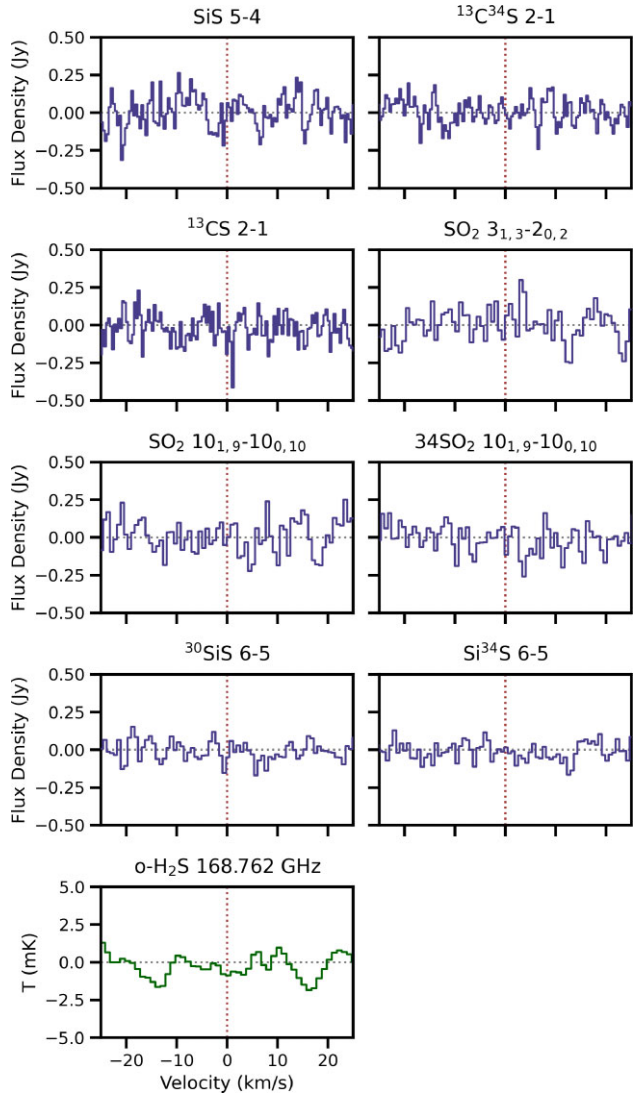


**Figure 1.** Spectra obtained from ALMA (blue) and APEX (green) for each of the transitions listed in Table 1. No spectral lines are detected. All spectra have been adjusted for the system velocity  $V_{\text{LSRK}} = 5.7 \text{ km s}^{-1}$ .

### 3 MODELLING

Our goal is to use the observational data outlined in the previous section to constrain the abundance of volatile sulfur-bearing species in HD 100546, and determine the radial profile of the total gas-phase elemental sulfur abundance  $S/H_{\text{gas}}$ .

We ran source-specific models using the 2D physical-chemical code DALI (Bruderer et al. 2012; Bruderer 2013). The code begins with a parametrized gas and dust density distribution and an input stellar spectrum, then uses Monte Carlo radiative transfer to determine the ultraviolet (UV) radiation field and dust temperature. This provides an initial guess for the gas temperature, which begins an iterative process in which the gas–grain chemistry is solved time-dependently. We let the chemistry evolve to 5 Myr to match the best estimate for the age of the disc. Finally, the raytracing module is used to obtain spectral image cubes, line profiles, and disc-integrated line fluxes.

The models presented in this paper are based on the HD 100546 disc model from Keyte et al. (2023), with some minor adjustments to improve the fit. See that work for a full description of the fitting procedure. Here, we briefly restate the key features of the model. A description of the updates and fiducial model parameters are given in Appendix B.

#### 3.1 Disc parameters

The disc structure is fully parametrized, with a surface density that follows the standard form of a power law with an exponential taper:

$$\Sigma_{\text{gas}} = \Sigma_c \cdot \left( \frac{r}{R_c} \right)^{-\gamma} \exp \left[ - \left( \frac{r}{R_c} \right)^{2-\gamma} \right], \quad (1)$$

where  $r$  is the radius,  $\gamma$  is the surface density exponent,  $\Sigma_c$  is some critical surface density, and  $R_c$  is some critical radius, such that the surface density at  $R_c$  is  $\Sigma_c/e$ . The scale height is then given by:

$$h(r) = h_c \left( \frac{r}{R_c} \right)^\psi, \quad (2)$$

where  $h_c$  is the scale height at  $R_c$ , and the power-law index of the scale height,  $\psi$ , describes the flaring of the disc.

$\Sigma_{\text{gas}}$  and  $\Sigma_{\text{dust}}$  extend from the dust sublimation radius ( $R_{\text{sub}}$ , defined as the inner edge of the model domain) to the edge of the disc ( $R_{\text{out}}$ ), and can be varied independently inside the cavity radius  $R_{\text{cav}}$  with the multiplication factors  $\delta_{\text{gas}}$  and  $\delta_{\text{dust}}$ .

The gas-to-dust ratio is denoted  $\Delta_{\text{g/d}}$ . Dust settling is implemented by considering two different populations of grains: small grains (0.005–1  $\mu\text{m}$ ) and large grains (0.005–1 mm). The vertical density structure of the dust is such that large grains are settled towards the midplane, prescribed by the settling parameter  $\chi$ :

$$\rho_{\text{dust, large}} = \frac{f \Sigma_{\text{dust}}}{\sqrt{2\pi} r \chi h} \exp \left[ - \frac{1}{2} \left( \frac{\pi/2 - \theta}{\chi h} \right)^2 \right], \quad (3)$$

$$\rho_{\text{dust, small}} = \frac{(1-f) \Sigma_{\text{dust}}}{\sqrt{2\pi} r h} \exp \left[ - \frac{1}{2} \left( \frac{\pi/2 - \theta}{h} \right)^2 \right], \quad (4)$$

where  $f$  is the mass fraction of large grains and  $\theta$  is the opening angle from the midplane as viewed from the central star.

#### 3.2 Stellar parameters

The stellar spectrum was modelled by Bruderer et al. (2012) using dereddened Far Ultraviolet Spectroscopic Explorer and International Ultraviolet Explorer observations at UV wavelengths, and then extended to longer wavelengths using the B9V template of Pickles

(1998). The stellar luminosity is  $36 L_\odot$  (Kama et al. 2016b). The X-ray spectrum was characterized as a thermal spectrum with a temperature of  $7 \times 10^7$  K over the 1–100 keV energy range, with an X-ray luminosity of  $L_X = 7.94 \times 10^{28}$  erg s $^{-1}$ .

#### 3.3 Chemical network

The chemical network used in our model is based on a subset of the UMIST 06 (Woodall et al. 2007) network. It consists of 131 species (including neutral and charged polycyclic aromatic hydrocarbons (PAHs)) and 1721 individual reactions. The code includes  $H_2$  formation on dust, freeze-out, thermal desorption, hydrogenation, gas-phase reactions, photodissociation and -ionization, X-ray induced processes, cosmic ray induced reactions, PAH/small grain charge exchange/hydrogenation, and reactions with vibrationally excited  $H_2$ . Non-thermal desorption is only included for a small number of species (CO, CO<sub>2</sub>, H<sub>2</sub>O, CH<sub>4</sub>, NH<sub>3</sub>). For grain surface chemistry, only hydrogenation of simple species is considered (C, CH, CH<sub>2</sub>, CH<sub>3</sub>, N, NH, NH<sub>2</sub>, O, OH, S, and HS). The details of these processes are described more fully in Bruderer et al. (2012). Of particular relevance to this study, the network includes reactions for 38 sulfur-bearing species, including all those listed in Table 1. The various isotopologs are not included as separate species, but abundances are computed using scaling relations based on typical interstellar-medium isotope ratios (Wilson & Rood 1994). Initial elemental abundances are listed in B2.

### 4 MODELLING RESULTS

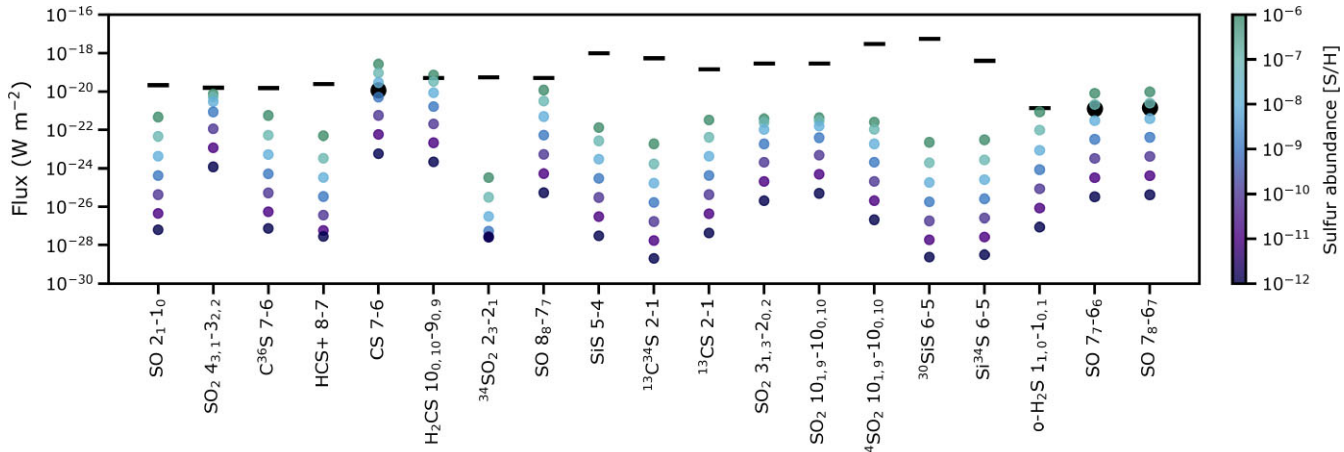
In order to model emission from sulfur-bearing species in HD 100546, we consider two broad scenarios. Firstly, a best-fitting disc-averaged sulfur abundance, and secondly, a sulfur abundance profile which includes both radial and azimuthal variations.

#### 4.1 Best-fitting disc-averaged sulfur abundance

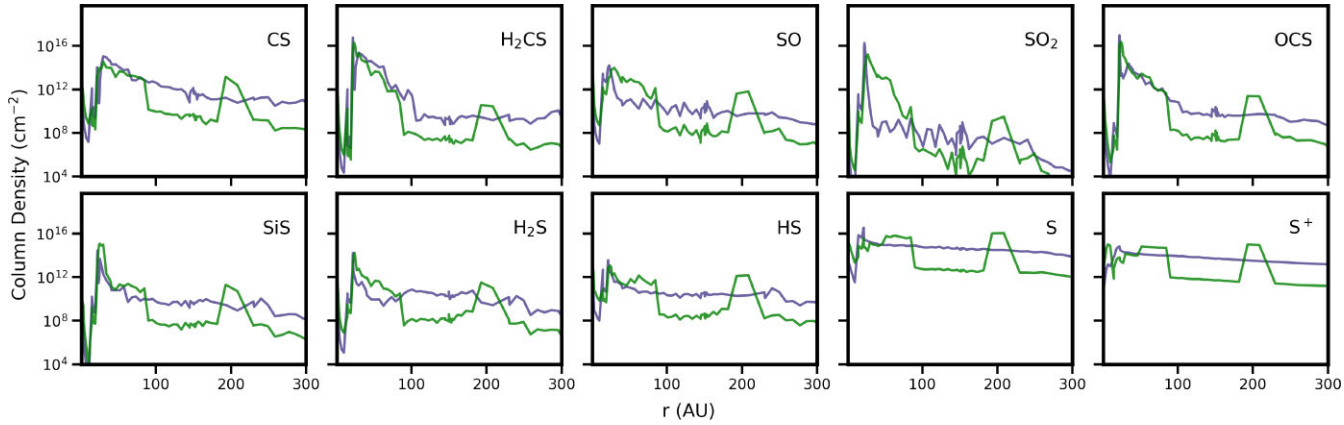
As step one, we assume a constant volatile sulfur abundance across the entire disc. It is initialized as entirely gas phase ( $S/H_{\text{gas}}$ ), though the code allows species formed in the gas to freeze out if local conditions mandate it. A constant global elemental abundance mimics the approach previously employed in prior analyses of  $C/H_{\text{gas}}$  and  $O/H_{\text{gas}}$  in the HD 100546 disc (Bruderer et al. 2012; Kama et al. 2016b). We ran models covering a wide range of sulfur abundances  $S/H$  from  $10^{-12}$  to  $10^{-6}$ . All other disc parameters remain fixed.

Fig. 2 shows the disc-integrated fluxes extracted from our models, alongside the observational detections and upper limits derived in Section 2. Volatile sulfur is found to be severely depleted in the HD 100546 disc, with the CS detection indicating a best-fitting value of  $\sim 5 \times 10^{-9}$  and the SO detections indicating a best-fitting value of  $\sim 5 \times 10^{-8}$ . This apparent contradiction is discussed in the next section. The upper limits of the remaining transitions provide no further constraints. These results suggest that the total amount of sulfur in the gas phase is depleted from the canonical cosmic value by at least two orders of magnitude.

Taking  $S/H = 10^{-8}$  as a fiducial value, we extracted column densities for ten key sulfur-bearing species: CS, H<sub>2</sub>CS, SO, SO<sub>2</sub>, OCS, SiS, H<sub>2</sub>S, HS, atomic S, and S<sup>+</sup>, shown in Fig. 3 (purple lines). All of the molecular species display similar morphological radial variations. Column densities peak within the inner dust ring at  $\sim 22$  au, then fall off in the outer disc, with varied slopes. The atomic S and S<sup>+</sup> column densities vary much more smoothly, remaining consistently high ( $\gtrsim 10^{14}$  cm $^{-2}$ ) well into the outer disc. We present



**Figure 2.** Disc-integrated fluxes for each of the transitions listed in Table 1. Observations are shown in black (where a circle represents a detection and a horizontal line is an upper limit). Model values are shown as coloured circles, where colours denote the initial sulfur abundance used in a given model.



**Figure 3.** Column densities for key sulfur-bearing species, extracted from our models. Purple lines show results for our best-fitting model using a single global sulfur abundance ( $S/H = 10^{-8}$ ). Green lines show results for our model using a radially varying sulfur abundance profile.

2D abundance maps for each of these species, in both the gas- and ice-phase, in Appendix C.

#### 4.2 Radially varying sulfur abundance

The models outlined in the previous section provide an estimation of the volatile sulfur abundance across the entire disc. However, fitting to disc-integrated line fluxes does not allow us to place constraints on variations in the sulfur abundance at small spatial scales. HD 100546 is known to be highly structured, featuring a small inner dust disc ( $r \lesssim 1$  au), two broad millimetre dust rings, and at least two protoplanet candidates. We may then reasonably expect radial variations in the disc chemistry, linked to processes such as radial drift, dust trapping, complex grain surface chemistry, and non-thermal desorption of sulfur-bearing species, which are not explicitly treated in the DALI modelling code. Furthermore, we have also previously shown that the asymmetric emission morphology and spectral line profiles of both the CS 7–6 and SO  $7_7 - 6_6 + 7_8 - 6_7$  observations can be reproduced by a model that incorporates an azimuthal variation in the C/O ratio (Keyte et al. 2023). The model from that work uses  $C/O = 0.5$  throughout most of the disc, except for a  $60^\circ$  radial arc on the western side of the disc, where the C/O ratio is elevated ( $=1.5$ ). These complexities, which are not accounted for in our ‘disc-averaged sulfur abundance’ model, may explain why

there is a discrepancy in the best-fitting value for  $S/H$  obtained by matching the CS and SO detections.

In this section, we use the SO  $7_7 - 6_6$ , SO  $7_8 - 6_7$ , and CS 7–6 observations to undertake a more detailed analysis of the sulfur abundance profile, fitting for both radial and azimuthal variations. We begin by deprojecting the SO  $7_7 - 6_6$ , SO  $7_8 - 6_7$ , and CS 7–6 integrated intensity maps, in order to extract radial intensity profiles. For each species, we extract a profile that is azimuthally averaged across the entire extent of the disc, ignoring the small region in which the C/O ratio is locally elevated. To begin with, we focus only on fitting these profiles, treating the region where C/O is elevated separately later. The profiles obtained from the two SO transitions are stacked to form a single profile.

Fig. 4 (top row) shows the SO and CS radial intensity profiles extracted from the observations, alongside profiles extracted from our models using a range of initial sulfur abundances  $S/H$  from  $10^{-6}$  to  $10^{-9}$ . The models have been convolved with a beam of the same size as the observations for a better comparison. The observed SO radial profile peaks at the edge of the inner dust ring, and gradually decreases before sharply falling off at  $\sim 125$  au. A second region of high abundance is observed in the outer disc between  $\sim 150$ – $250$  au, roughly coincident with the outer millimetre dust ring. The observed CS profile peaks at the location of the host star, and falls off smoothly to the outer disc. None of our models are able

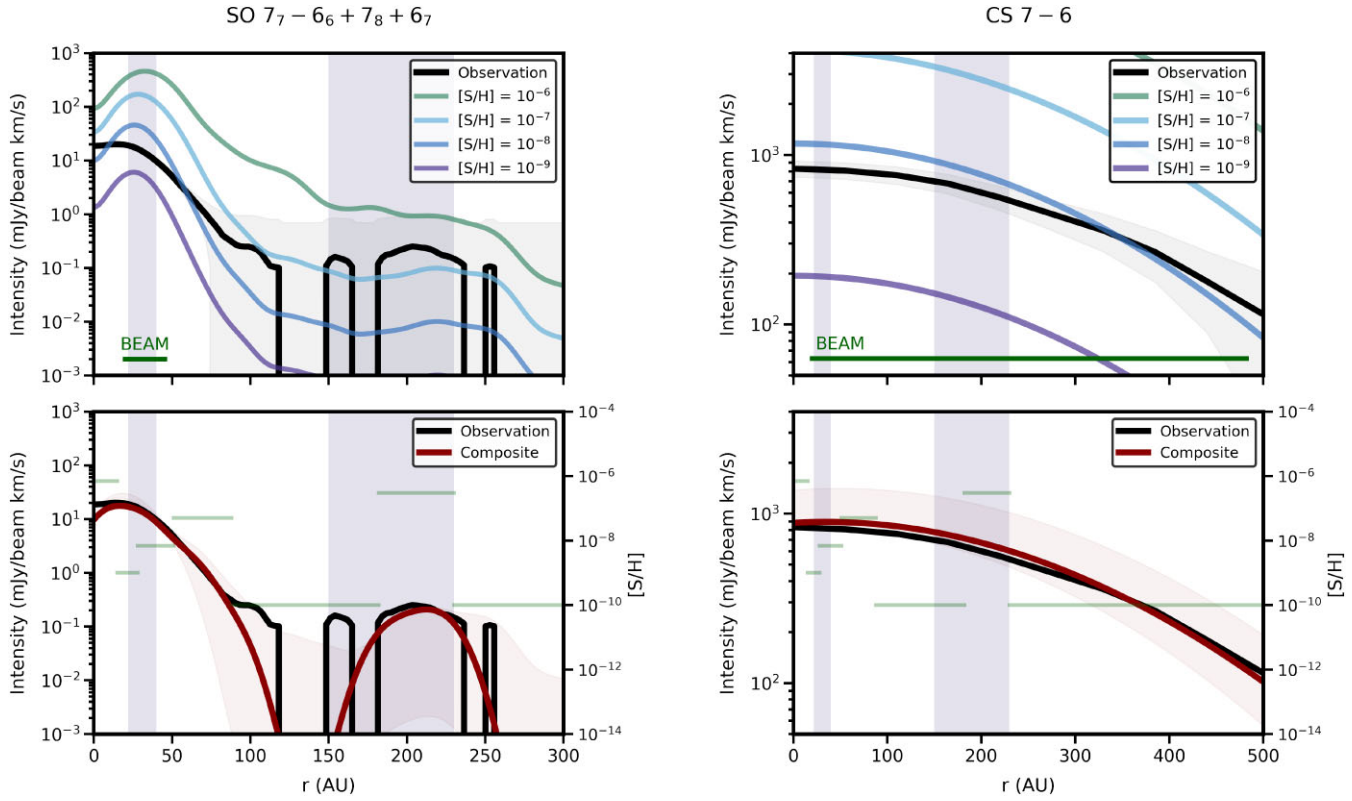


**Figure 4.** Top row: Radial intensity profiles extracted from deprojected integrated intensity maps, azimuthally averaged across the entire disc except in the region where C/O is locally elevated. Observations (black, with uncertainties shaded in grey) and models using a range a sulfur abundances (coloured). The semimajor axis of the beam is denoted by the horizontal bar in the lower part of the panel. Shaded blue columns denote the locations of prominent millimetre dust rings. Bottom row: radial intensity profiles extracted from our composite model (red). Horizontal green lines signify the radial regions in which models were spliced together, arranged to match the corresponding sulfur abundance on the secondary y-axis. Shaded red regions denote the space covered by models computed using the  $\pm 1\sigma$  intervals from the posterior distributions.

to simultaneously reproduce the SO or CS emission morphology. Models which reproduce the SO emission in the inner disc fail to reproduce the significant emission peak in the outer region, while models which include significant flux in the outer disc overpredict emission inside of  $r \sim 150$  au.

We constructed a composite model by dividing the radial intensity profiles into a pre-defined number of radial regions, fitting each region with a model that has a sulfur abundance S/H from  $10^{-12}$  to  $10^{-6}$ . In order to efficiently sample the parameter space, we adopted a Markov Chain Monte Carlo (MCMC) approach, making use of the PYTHON package EMCEE (Foreman-Mackey et al. 2013). The radial locations at which models are spliced together are treated as free parameters, with uniform priors ranging between 0 and 300 au. The models applied to each region are free parameters drawn from a discretized set of 20 models covering the allowed range of initial sulfur abundances. The SO and CS profiles are fit simultaneously using the same set of free parameters.

In each MCMC iteration, models are first spliced together, then convolved with a beam to match the observation. The goodness of fit of the convolved profile is determined using the log-likelihood function:

$$L = -\frac{1}{2} \sum \left( \frac{y_{\text{obs}} - y_{\text{model}}}{\sigma} \right)^2, \quad (5)$$

where  $y_{\text{obs}}$  are the observational data points,  $y_{\text{model}}$  are the model data points, and  $\sigma$  are the uncertainties on the observations.

We ran the MCMC multiple times, each time using a different number of pre-defined radial regions. We found that eight regions were sufficient to describe variations in the intensity profiles. Using more than eight regions resulted in at least two neighbouring regions sharing the same initial sulfur abundance. In each case, we ran the MCMC for 40 000 steps (excluding 1000 burn-in steps), using 30 walkers. The best-fitting composite model is shown in Fig. 4 (lower panel). Horizontal green lines denote the radial extent of each model used to form the composite profile, with the vertical position of each line denoting the sulfur abundance used in that particular model (secondary y-axis). The shaded red area denotes the space covered by models computed using the  $\pm 1\sigma$  intervals from the posterior distributions.

The composite model indicates that the volatile sulfur abundance varies by at least  $\sim 3$  orders of magnitude throughout different radial regions of the disc. Within the central cavity, the gas-phase sulfur abundance is found to be relatively high ( $S/H \sim 7 \times 10^{-7}$ ), then falls off dramatically inside the inner dust ring ( $S/H \sim 1 \times 10^{-9}$ ). Immediately outside of the dust ring, another region of relatively high abundance is identified ( $S/H \sim 5 \times 10^{-8}$ ), which we note is broadly coincident with the proposed location of the protoplanet HD 100546 b (Currie et al. 2015; Quanz et al. 2015). We discuss this further in Section 5. A third region of relatively high abundance ( $S/H \sim 3 \times 10^{-7}$ ) is identified between 180–230 au, broadly coincident with the outer dust ring. This is bounded on both sides by regions of low abundance ( $S/H \sim 10^{-10}$ ), corresponding to regions where large dust grains are highly depleted. The best-fitting model appears to be missing SO emission in the region between  $\sim 100$ –125 au. To

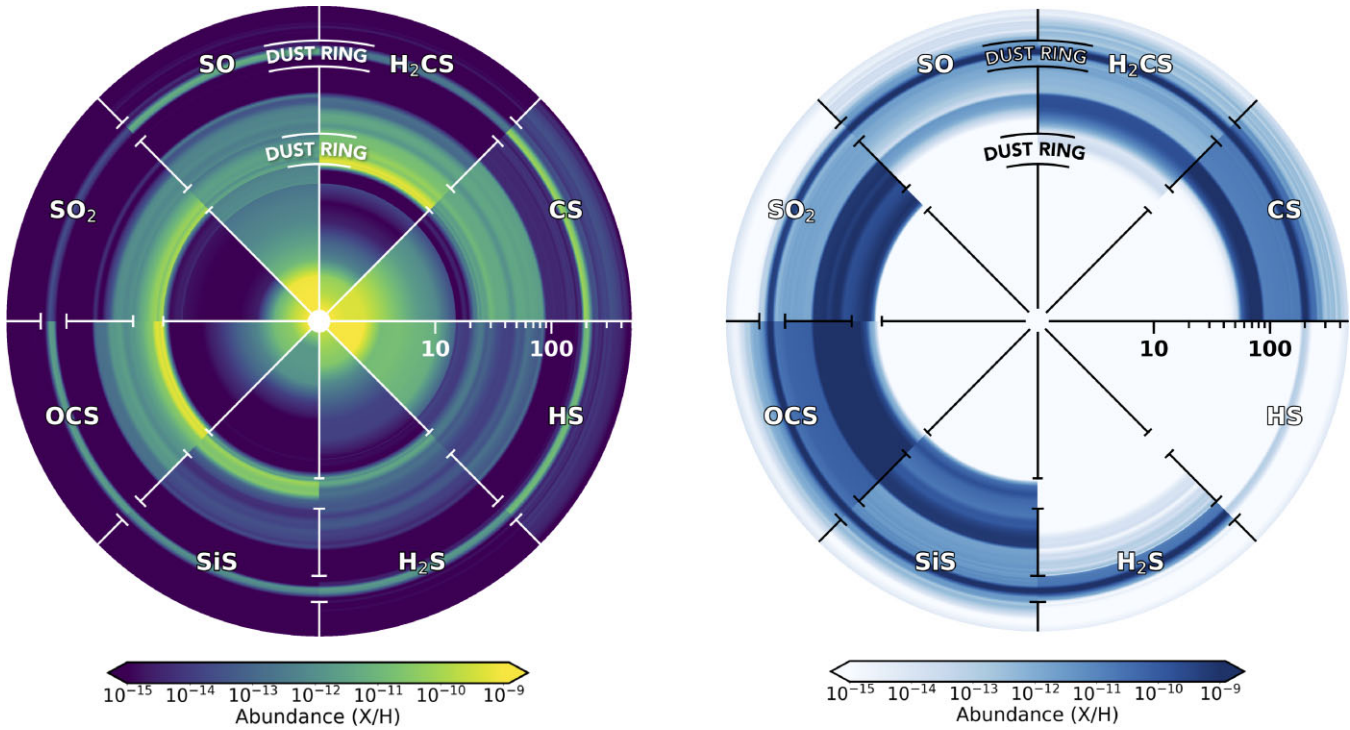


**Figure 5.** Vertically integrated molecular abundances extracted from our composite model, as a function of radius. Gas phase (left) and ice-phase (right).

investigate this, we manually spliced together a model using a higher sulfur abundance in these regions, matching the SO intensity profile by eye. While this led to a better-fitting SO profile, it caused the CS radial profile to be significantly overpredicted. Possible explanations for this discrepancy are discussed in Section 5.

Having determined the radial gas-phase sulfur abundance profile throughout most of the disc, we now check for consistency by ensuring that our composite model also fits the small region in which the gas-phase C/O ratio is locally elevated. Following the procedure outlined in Keyte et al. (2023), we compute the abundances within this region, finding the composite model to be a reasonable match to the data (Appendix D). In this region, the observed SO emission tapers off dramatically at  $\sim 75$  au, compared to  $\sim 120$  in the rest of the disc. The modelling SO emission also tapers off more quickly in this region, although not to the same degree, cutting off abruptly at  $\sim 100$ . In the outer disc, the modelled emission is slightly more extended than the observed emission outside of the second dust ring. The modelled CS emission matches the observation extremely well, reproducing the elevated flux in the outer disc. Since both regions can be well fitted using the same radially varying sulfur abundance profile, we focus only on the large region of the disc where  $\text{C}/\text{O} = 0.5$  for the remainder of the study, unless otherwise stated.

We present a side-by-side comparison of the modelled molecular abundances extracted from our composite model in Fig. 5, for each of the gas- and ice-phase sulfur bearing species. Individual 2D abundance maps are presented in Appendix C.

## 5 DISCUSSION

### 5.1 Total elemental gas-phase sulfur abundance

We have shown that volatile sulfur is highly depleted in the HD 100546 protoplanetary disc, regardless of whether the abundance

is determined as a single global value or as a radially varying gas-phase elemental S/H ratio, which is possible using the full information content of the available data.

Using models with a single sulfur abundance across the entire disc, we find  $\text{S}/\text{H} \lesssim 5 \times 10^{-8}$ , over two orders of magnitude lower than the canonical cosmic value. This level of depletion is consistent with the ‘highly depleted’ S-abundance values used in many previous studies. Modelling of the discs around MWC 480, LkCa15, and DM Tau by Dutrey et al. (2011), for example, showed that an initial abundance value of  $\text{S}/\text{H} = 8 \times 10^{-9}$  was required to reproduce the CS and SO column densities. Similarly, a study by Le Gal et al. (2019) showed that the observed CS column densities in MWC 480 and LkCa15 could be reproduced with a model using an initial value of  $\text{S}/\text{H} = 8 \times 10^{-8}$ . In both studies, models were not able to fully reproduce the inferred abundances of all sulfur-bearing species, leading to an overprediction of the  $\text{H}_2\text{S}$  abundance (Dutrey et al. 2011) or underprediction of the  $\text{H}_2\text{CS}$  column density (Le Gal et al. 2019). Such discrepancies are thought to be related to missing reaction pathways, rather than an undepleted sulfur reservoir. Laboratory studies have shown that  $\text{H}_2\text{CS}$  can form as an intermediate product via a reaction with  $\text{H}_2\text{S}$  and atomic C, for example (Galland et al. 2001). More studies are needed to develop an improved understanding of sulfur chemistry and more complex chemical networks.

The precise impact of missing reaction pathways on modelled abundances is difficult to predict. One such result may be related to our finding that a single sulfur abundance across the entire disc does not adequately reproduce the  $\text{SO } 7_7 - 6_6 + 7_8 - 6_7$  and  $\text{CS } 7 - 6$  radial intensity profiles. To better understand why the sulfur abundance may be subject to radial variations, we consider the fraction of the total sulfur budget split between refractories, ices, and gas. Using the radial abundance profile derived in Section 4.2, we plot the proportion of sulfur held in each of these three reservoirs as a function of radius,

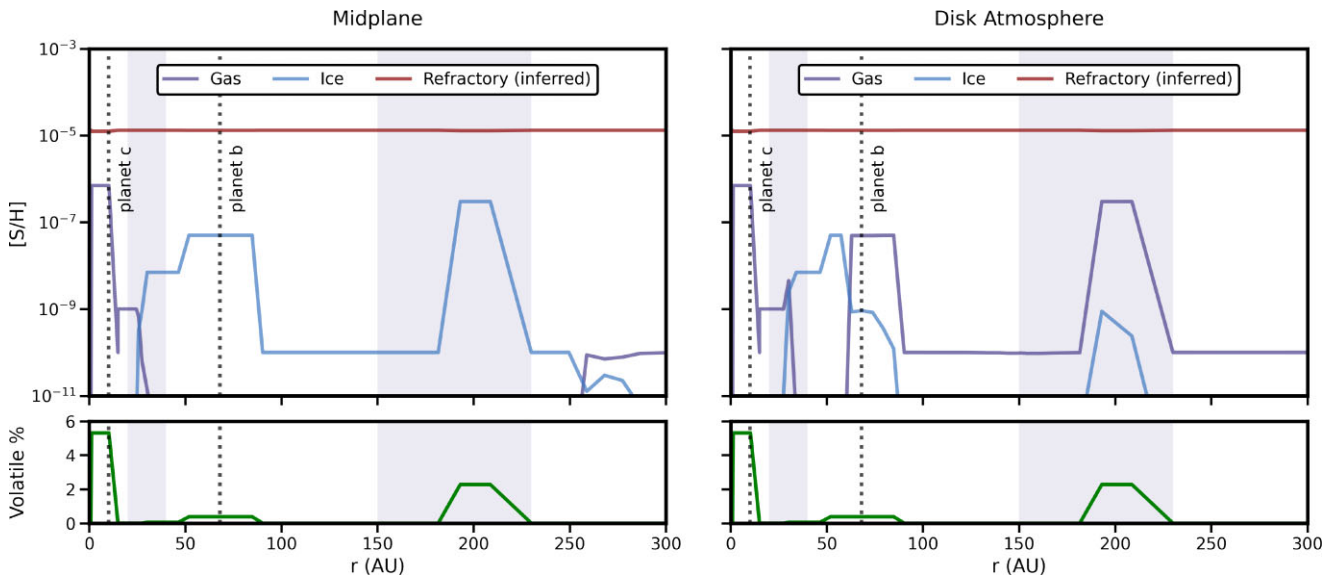


**Figure 6.** Total elemental sulfur abundance of refractories, ices, and gas, as a function of radius. The gas and ice-phase abundances are extracted from our composite model, which uses a radially varying sulfur abundance (Section 4.2). The abundance of refractory sulfur-bearing species is inferred from the difference between the cosmic abundance and the total volatile abundance (ice + gas) extracted from the model. Shaded columns represent the location of millimetre dust rings. *Left:* midplane abundances. *Right:* abundances in the warm molecular layer of the disc atmosphere between  $z/r = 0.2 - 0.3$ . The lower panels in each column show the total amount of volatile sulfur (gas + ice) expressed as a percentage of total sulfur.

at both the midplane (Fig. 6, left) and in the warm molecular layer of the disc atmosphere (Fig. 6, right). Values for gas and ice are the total sum of all sulfur-bearing gas and ice species extracted from our model. The abundance of refractory sulfur-bearing species is inferred from the difference between the cosmic abundance and the total volatile abundance (ice + gas) extracted from the model.

In the disc midplane, almost all volatile sulfur is locked up into ices beyond  $r \sim 30$  au. The inside edge of the inner dust ring can be considered a transition region, with all volatile sulfur returning to the gas phase within the inner cavity ( $r \lesssim 22$  au). In the disc atmosphere, the transition from gas to ice at the cavity edge is still apparent, but another transition region is evident in the outer disc at  $r \sim 60$  au, where the majority of the volatile sulfur returns to the gas.

The correlation between phase transitions/abundance peaks and the location of prominent millimetre dust rings is suggestive of an underlying connection with grain chemistry or ice adsorption/desorption in both the inner and outer disc. Booth et al. (2023b) propose that SO emission from the inner disc may be partly related to thermal desorption of sulfur-rich ices at the edge of the inner dust cavity, a scenario which is supported by the sharp increase in gas-phase sulfur at the cavity boundary in our model. The same study also suggested that this emission may be due to shocked gas emanating from a circumplanetary disc around a newly forming planet. This scenario is supported by the fact that the peak in the gas-phase sulfur abundance is located inside the cavity, rather than coincident with the dust ring itself. If this is the case, the sulfur abundance in the inner cavity derived from our fit to the SO radial intensity profile may not be a reliable indicator of the abundance of other sulfur-bearing species in this region. Alternatively, the high gas-phase sulfur abundance within the cavity may be linked to the inward drift and sublimation of sulfur-bearing icy grains, which is not incorporated in our dynamically static model.

In the outer dust ring, temperatures are too low for thermal desorption, and the increase in gas-phase volatile sulfur must be driven by some other mechanism. One possible explanation for this is non-thermal desorption from icy grains (Booth et al. 2023b), a

scenario which is consistent with rings of H<sub>2</sub>CO emission observed in the outer disc in a number of other sources (Rivière-Marichalar et al. 2021). Our models do not include non-thermal desorption of any sulfur-bearing species; if a significant fraction of ices are being desorbed in the outer disc, then a lower volatile sulfur abundance than that inferred from our MCMC fitting could reproduce the gas-phase abundance, with a smaller fraction of the total volatiles held in ices.

Taking all radial variations into account, we find that the *total* amount of sulfur locked into volatiles accounts for  $\sim 0.01 - 5.3$  per cent of the cosmic abundance, dependent on radius. This is broadly in agreement with upper limits on refractory sulfur described in Kama et al. (2019;  $< 93$  per cent of total sulfur), but suggests that an even higher proportion of sulfur is locked into refractories throughout large regions of the disc. The abundance of volatile sulfur in the disc on scales we are sensitive to is also significantly below the sulfur abundance in material currently accreting onto the central star (the total S/H in the accreting material is  $\sim 3$  times below solar; Kama et al. 2016b, 2019). This is consistent with a substantial fraction being transported through the large inner cavity either in small grains or as a semirefractory reservoir which evaporates at the  $\gtrsim 100 - 200$  K temperatures of the main dust ring.

## 5.2 Main volatile sulfur carriers

In this section, we use abundances obtained from our chemical model to determine the major volatile sulfur carriers in HD 100546 at small spatial scales. Astrochemical models have long predicted dominant carriers in discs to include H<sub>2</sub>S, SO, SO<sub>2</sub>, and CS (e.g. Pasek et al. 2005). Observations of comets show that H<sub>2</sub> is indeed a major volatile sulfur carrier (Calmonte et al. 2016), which is thought to be due to its preferential formation via hydrogenation of atomic sulfur on grain surfaces (Charnley 1997):



while atomic H can abstract H from H<sub>2</sub>S:



and then subsequently reform H<sub>2</sub>S via reaction (7). Approximately 4 per cent of the H<sub>2</sub>S produced in this way will be released into the gas phase via chemical desorption (Oba et al. 2018; Furuya et al. 2022; Santos, Linnartz & Chuang 2023).

Indeed, H<sub>2</sub>S has the highest inferred abundance of any *ice-phase* sulfur carrier in star-forming regions, although still a factor of  $\geq 10$  lower than the cosmic value (van Dishoeck & Blake 1998). Frozen-out H<sub>2</sub>S can be released from grain surfaces by photodesorption in regions dominated by high-UV radiation, although additional photochemistry can lead to destruction via dissociation (Jiménez-Escobar & Muñoz Caro 2011). High-solid-phase H<sub>2</sub>S abundances do not therefore necessarily imply a large gas-phase reservoir. In recent years, this has become apparent in observations, with chemical models routinely overpredicting inferred abundances. Phuong et al. (2018), for example, used the chemical code Nautilus to model H<sub>2</sub>S detected in GG Tau, overpredicting the inferred column density by a factor of  $\sim 10$ . In that case, however, the detection itself is thought to be related to the high disc mass rather than low levels of sulfur depletion. Similarly, a study of H<sub>2</sub>S detected in AB Aur suggests that 99.99 per cent of H<sub>2</sub>S is locked into grain surfaces, and only  $\sim 9.5$  per cent of total sulfur is available for gas-phase chemistry (Rivière-Marichalar et al. 2021).

Among other sulfur-bearing molecular species, CS and H<sub>2</sub>CS are the most widely detected in discs (VanderPlas 2018; Teague et al. 2016; Semenov et al. 2018; Le Gal et al. 2019, 2021). Conversely, the oxygen-bearing species SO and SO<sub>2</sub> have only been detected in a handful of sources (Guilloteau et al. 2016; Fuente et al. 2017; Booth et al. 2021). Such observations are consistent with the observed overall depletion of volatile oxygen and an elevated C/O ratio in many discs (Miotello et al. 2019; Zhang, Bosman & Bergin 2020; Bosman et al. 2021). Typically, inferred abundances of CS and H<sub>2</sub>CS account for only a small fraction of total sulfur (<1 per cent), indicating large refractory or unknown volatile reservoir.

It is insightful to compare the outputs of our model to molecular abundances predicted by previous studies. To aid the discussion, we focus on comparing the abundances as a function of height, at four fixed radial locations in the disc (Fig. 7). Each radial location is chosen to be representative of particular regions where we might expect large variations in the chemistry: the inner dust cavity ( $r = 5$  au), inner dust ring ( $r = 25$  au), outer gap ( $r = 100$  au), and outer dust ring ( $r = 200$  au). For clarity, we only display the five most abundant species in each region. Note that in the upper disc atmosphere, all volatile sulfur is in the form of atomic S and/or S<sup>+</sup>. The precise location where atomic sulfur becomes ionized varies as a function of radius, but is typically at  $z/r \sim 0.10$  in the inner dust cavity, and  $z/r \sim 0.25$  in the outer disc. The rest of this discussion therefore focuses on the volatile carriers at the midplane and in the warm molecular layer only.

Within the inner cavity, a small molecular reservoir exists close to the midplane, pre-dominantly as HS, CS, and SO, although these account for less than 0.1 per cent of the total volatile sulfur budget. Gas-phase molecular carriers become much more abundant within the inner dust ring between  $r \sim 22$ –40 au. At the midplane, almost all volatile sulfur is locked into gaseous H<sub>2</sub>CS or OCS ( $\sim 55$  per cent and 40 per cent respectively). While H<sub>2</sub>CS is now routinely observed in discs, OCS has yet to be detected and future observations will be needed to assess its potential as a primary gas-phase sulfur reservoir. Further up in the disc atmosphere, OCS and H<sub>2</sub>CS abundances fall

off sharply, with SO<sub>2</sub> taking over as the main S-carrier, accounting for  $\sim 90$  per cent of total S volatiles between  $z/r \sim 0.15$ –0.25.

In the outer dust gap at  $r = 100$  au, dust temperatures reach  $\sim 40$  K in the midplane, and  $> 99.9$  per cent of volatile sulfur is frozen out on to grain surfaces. In the midplane, the major ice-phase sulfur carrier is OCS, accounting for  $\sim 60$  per cent of all volatile sulfur below  $z/r \lesssim 0.25$ . Most of the remaining volatile sulfur in the midplane is locked into CS ice. In the disc atmosphere, the major ice-phase reservoirs are SO<sub>2</sub> and SiS. Quantifying the presence of such ices in discs is not straightforward, but we may infer the likely reservoirs through observations of comets, which represent pristine remnants of the primordial solar disc. Detections of OCS from comets are relatively common, with measured abundances ranging from  $\sim 0.02$ –0.5 per cent relative to water (e.g. Dello Russo et al. 1998; Le Roy et al. 2015). OCS ice was also recently tentatively detected in the disc around HH 48 NE with JWST (Sturm et al. 2023). Conversely, SO<sub>2</sub> has only two cometary detections, but the inferred abundances are similar to that of OCS (Bockelée-Morvan et al. 2000; Le Roy et al. 2015). The apparent lack of SO<sub>2</sub> detections may be tied to the relative ease with which it is photodissociated, with the photodissociation product SO being much more widely detected (e.g. Bockelée-Morvan et al. 2000; Biver et al. 2006, 2015; Le Roy et al. 2015). Ice reservoirs may also be inferred from gas-phase emission in discs. Gas-phase SO<sub>2</sub> detected towards the Oph IRS 48, for example, is thought to originate from sublimation of ices at the edge of a dust cavity, with the bulk of the ice reservoir coincident with millimetre dust grains (Booth et al. 2021). The presence of SiS ice in our model is more challenging to explain. Silicon is typically considered to be highly depleted in discs, with chemical models using abundances of Si/H  $\sim 10^{-8}$ , based on low metal abundances inferred from studies of interstellar cloud chemistry (Graedel, Langer & Frerking 1982). Our modelling of HD 100546, however, constrains the total elemental gas-phase silicon abundance in this disc to Si/H =  $5 \times 10^{-7}$ , using upper limits of the HCO<sup>+</sup> 4–3 disc-integrated line flux. This constraint is due to the impact that electrons from ionized metals (Si, Mg, Fe) have on the disc ionization structure, with high metal abundances leading to suppression of HCO<sup>+</sup> (Fromang, Terquem & Balbus 2002). Further observations and modelling will be required to better constrain the silicon content, but if the abundance is considerably lower than our modelled value then the constraint from SiS is loosened and a significant amount of additional elemental sulfur may be available for incorporation into other species.

Within the outer dust ring between  $r \sim 150$ –230 au, molecular ices are dominant at the midplane. OCS and CS are still the major carriers, although H<sub>2</sub>S ices are also prominent in a narrow region, with abundances that fall off rapidly with height. Further up in the disc atmosphere, OCS ices persist, but CS ice abundances fall off and SiS ices become abundant above  $z/r \sim 0.1$ . Here, the low densities allow external far ultraviolet (FUV) radiation to penetrate more deeply and locally increase the temperatures such that a small amount of sulfur-bearing molecules can exist in the gas-phase. These are predominantly in the form of HS, SO, and CS, although combined account for only  $\sim 0.2$  per cent of sulfur-bearing volatiles.

In summary, our results provide new constraints on the major volatile sulfur carriers in protoplanetary discs. The identification of OCS as a major ice-phase reservoir highlights the need for more high-resolution observations of sulfur-bearing species. Conversely, the low relative abundance of gas-phase H<sub>2</sub>S in our models places doubt on the consensus that it is the major volatile sulfur carrier in planet-forming environments. The H<sub>2</sub>S ice reservoir is also small, by comparison to the other sulfur-bearing molecular ices. To assess the impact of initial conditions on the H<sub>2</sub>S

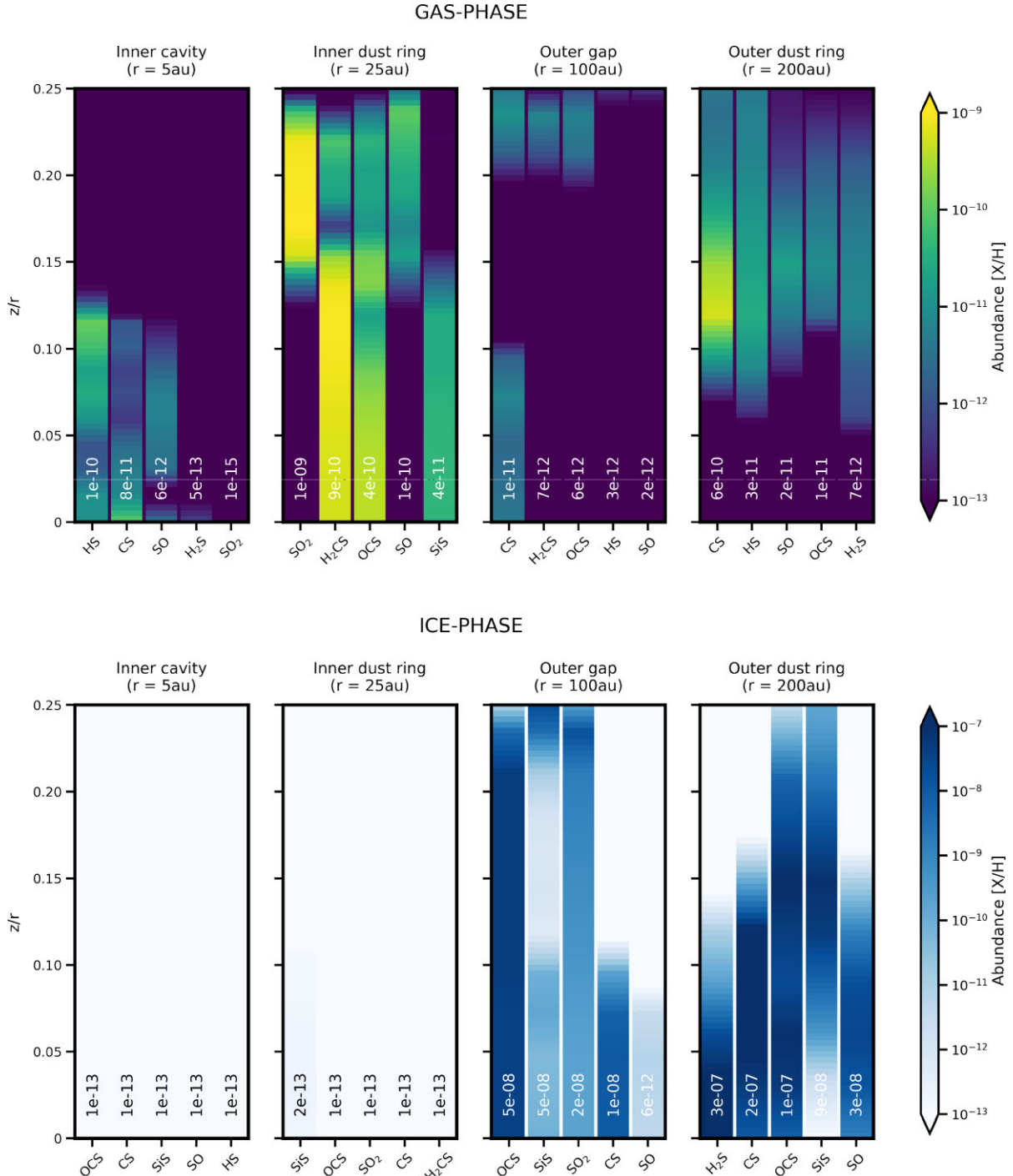


**Figure 7.** Vertical abundance profiles for the main molecular sulfur carriers extracted from our fiducial model, at four fixed radial locations ( $r = 5, 25, 100, 200$  au). Only the five most abundant species in each region are shown. In each panel, species are ordered by peak abundance (X/H), with the peak value annotated in the respective column. *Top panel: gas-phase abundances. Bottom panel: ice-phase abundances.*

abundance, we ran a second grid of models in which all sulfur was initialized in the form of  $\text{H}_2\text{S}$  ice, rather than atomic gas-phase S. We found no considerable difference in the abundances obtained from these models, compared to the fiducial models presented in Section 4, suggesting that the sulfur chemistry reaches a steady state within the 5 Myr chemical time-scale. One possible explanation for the low  $\text{H}_2\text{S}$  abundance and large OCS ice reservoir is the lack of grain chemistry in our chemical network. Experimental studies have shown that reactions of solid OCS

with atomic hydrogen can produce OCS–H radicals, which further react with H atoms to produce  $\text{H}_2\text{S}$  and CO (Nguyen et al. 2021):



Solid H<sub>2</sub>S can then be released back into the gas phase via chemical desorption, as described above. Experimental studies also show an efficient depletion of H<sub>2</sub>S due to H-atom abstraction reactions forming HS, which could associate with other radicals/molecules to form S-bearing species or chemically desorb into the gas phase (Oba et al. 2018; Santos, Linnartz & Chuang 2023). However, we note that our findings on the importance of OCS and relatively low abundance of H<sub>2</sub>S in the HD 100546 disc mirror those from early solid-state transmission spectroscopy of protostellar ices using *JWST*, which reach the same conclusion (McClure et al. 2023). Such results may be indicative of high levels of UV photoprocessing, which convert a significant amount of H<sub>2</sub>S ice to OCS (Jiménez-Escobar, Muñoz Caro & Chen 2014; Chen et al. 2015).

### 5.3 Implications for planets

Elemental abundance ratios in discs are promising tracers of planetary formation and migration pathways. The C/O ratio has received particular attention in studies of both discs and exoplanet atmospheres due to the high cosmic abundances of both carbon and oxygen, and the wealth of associated molecular carriers. Simple models relate C/O measured in exoplanet atmospheres to potential formation locations in discs based on the location of volatile molecular snowlines. In this approach, the gas-phase C/O is a step function which increases with distance from the host star (Oberg, Murray-Clay & Bergin 2011). Recent studies have expanded on this idea, showing that additional mechanisms can lead to both radial and azimuthal C/O variations at small spatial scales, which adds further complexity (Cleeves et al. 2018; Miotello et al. 2019; Zhang et al. 2019; Bosman et al. 2021). While the C/O ratio remains a powerful diagnostic tool, its utility as a tracer of planetary formation processes is limited, especially in cases where planets acquire the bulk of their carbon and oxygen beyond the CO<sub>2</sub> snowline. In recent years, the use of additional elemental abundance ratios has been explored to further constrain disc compositions and break degeneracies associated with the C/O ratio. Turrini et al. (2021), for example, showed that the C/N and N/O ratios can be used to constrain the extent of planetary migration, while the S/N ratio can be used as a reliable tracer of heavy element enrichment. Further, Hobbs, Shorttle & Madhusudhan (2022) used the C/H, O/H, and N/H ratios to predict connections between the atmospheric molecular abundances of hot Jupiters and their formation pathways. In this section, we explore the utility of the S/H ratio and its impact on planets in the HD 100546 disc, as well as its wider application to discs in general.

In HD 100546, multiple observations provide evidence for at least two giant planetary candidates within the disc; planet ‘b’ at  $r \sim 55$  au, and planet ‘c’ within the inner cavity at  $r \sim 13$  au. How might the composition of these planets’ atmospheres vary, based on the radial gas-phase S/H variations implied by our models? As we have shown, a region of elevated S/H<sub>gas</sub> in the outer disc appears broadly coincident with the outer millimetre dust ring, while another region of elevated S/H<sub>gas</sub> resides directly outside of the inner dust ring. The dust rings themselves are likely the products of planetary formation processes, and the interplay between the dust structure, gas composition, and materials accreted by planets will be complex and ever-evolving. It is important to highlight the fact that the vast majority of elemental sulfur (>94 per cent) is locked up into refractory materials, and the sulfur content of an exoplanet atmosphere will not only depend on the composition of the accreted gas, but the amount of sulfur returned to the gas phase from accreted solids. Gas giant envelopes can become enriched in this manner through a number of mechanisms,

including dissolution of pebbles/planetesimals during accretion, and core erosion/mixing (Hueso & Guillot 2003; Estrada et al. 2009). Some level of enrichment is to be expected, but placing precise constraints is challenging since dissolution and mixing are not well understood (Leconte & Chabrier 2013; Nettelmann et al. 2015; Moll et al. 2017). Studies of elemental enrichment in Jupiter’s atmosphere, for example, suggest that >50 per cent of the core has become dissolved in the envelope (Öberg & Wordsworth 2019). Such high levels of mixing may not be representative of the general exoplanet population, however, since it has been proposed that the distribution of heavy elements in Jupiter’s inner envelope could only come about through a collision which shattered Jupiter’s primordial core (Liu et al. 2019). Uncertainties on the levels of enrichment through core dissolution/mixing are particularly problematic for interpreting observations of sulfur-bearing species in exoplanet atmospheres, since almost all sulfur is tied up in refractory species.

Previous studies which propose the S/N ratio as direct tracer of planetesimal accretion, rely on the fact that most of the sulfur is incorporated into solids, while nearly all nitrogen is in gaseous N<sub>2</sub> (Turrini et al. 2021). The S/H ratio is analogous to the S/N ratio in this sense. The joint evaluation of S/N with independent measurements of metallicity allow further constraints to be placed on migration scenarios, with *in situ* formation characterized by stellar metallicity and stellar S/N, and extensive migration characterized by super-stellar metallicity and stellar S/N (Pacetti et al. 2022). In practice, observations and modelling of sulfur-bearing species in exoplanet atmospheres will need to consider the separate contributions from directly-accreted gas, and solids returned to the gas phase, in order to use S/N or S/H as reliable tracers of these mechanisms.

## 6 CONCLUSIONS

In this work, we presented new data from ALMA and APEX relating to volatile sulfur-bearing species in the HD100546 protoplanetary disc. We used a highly refined and disc-specific physical-chemical models to infer the total elemental sulfur content, and predict which species are the major carriers of volatile sulfur in the disc. Our main conclusions are:

- (i) We observed transitions of seven sulfur-bearing species towards HD 100546 with ALMA, in addition to an observation of H<sub>2</sub>S at 168.762 GHz with APEX. All species were undetected. We derived upper limits on the disc-integrated fluxes for all transitions.
- (ii) We used the physical-chemical disc modelling code DALI to determine the volatile sulfur abundance. Using simple models with a single sulfur abundance across the entire disc, we find volatile sulfur to be heavily depleted from the cosmic value by at least two orders of magnitude, S/H  $\lesssim 5 \times 10^{-8}$ , constrained by these upper limits and the previous detections of SO and CS
- (iii) Comparing our models to the SO 7<sub>7</sub> – 6<sub>6</sub> + 7<sub>8</sub> – 6<sub>7</sub> radial intensity profile from Booth et al. (2023b), we find that a single sulfur abundance across the entire disc does not adequately reproduce the observations. We used an MCMC approach to construct a composite model, finding that the sulfur abundance varies radially throughout the disc by at least three orders of magnitude.
- (iv) Radial variations in the sulfur abundance broadly coincide with the location of prominent millimetre dust rings and gaps. Models indicate that many of the sulfur-bearing molecules are particularly abundant inside the inner dust ring ( $r \sim 22$ –40 au), and coincident with the outer dust ring ( $r \sim 150$ –230 au). The total gas-phase sulfur abundance is high within the dust-depleted inner cavity, with most

sulfur in the form of atomic S or S<sup>+</sup>. SO and HS are most abundant molecular carriers with inner cavity.

(v) We determined the major volatile gas-phase sulfur carriers to include OCS, H<sub>2</sub>CS, and CS. We also infer the presence of a substantial OCS ice reservoir in the outer disc, alongside other molecular ices at lower abundance. H<sub>2</sub>S is found to have low abundances in both the gas- and ice-phases, in contrast to predictions from many previous astrochemical models.

(vi) The total amount of sulfur held in volatiles ranges from  $\sim$ 0.01–5.3 per cent, dependent on radius. The use of elemental ratios S/H and S/N as tracers of planetary formation is complicated by the uncertainties on the split between volatiles and refractories, and the level at which accreting refractories are processed into planetary atmospheres.

## ACKNOWLEDGEMENTS

LK acknowledges funding via a Science and Technology Facilities Council (STFC) studentship. KJC is grateful for the Dutch Research Council (NWO) support via a VENI fellowship (VI.Veni.212.296). LIC acknowledges support from NASA ATP 80NSSC20K0529, NSF AST-2205698, the David and Lucille Packard Foundation, the Research Corporation for Scientific Advancement Cottrell Scholar Award, and Heising-Simons grant 2022-3995. MND acknowledges the Swiss National Science Foundation (SNSF) Ambizione grant no. 180079, the Center for Space and Habitability (CSH) Fellowship, and the IAU Gruber Foundation Fellowship. KF is supported by JSPS KAKENHI grant nos. 20H05847 and 21K13967.

## DATA AVAILABILITY

The data presented here are from the ALMA Cycle 5 programme 2017.1.00885.S (principal investigator M. Kama). The raw data are publicly available from the ALMA archive. The reduced data and final imaging products are available upon reasonable request from the corresponding author. The ALMA data were reduced using CASA version 5.6.1-8, which is available at <https://casa.nrao.edu/>.

## REFERENCES

Altweig K. et al., 2022, *MNRAS*, 516, 3900

Ardila D. R., Golimowski D. A., Krist J. E., Clampin M., Ford H. C., Illingworth G. D., 2007, *ApJ*, 665, 512

Arun R., Mathew B., Manoj P., Ujjwal K., Kartha S. S., Viswanath G., Narang M., Paul K. T., 2019, *AJ*, 157, 159

Asplund M., Grevesse N., Sauval A. J., Scott P., 2009, *ARA&A*, 47, 481

Belitsky V. et al., 2018, *A&A*, 612, A23

Benisty M., Tatulli E., Ménard F., Swain M. R., 2010, *A&A*, 511, A75

Biver N. et al., 2006, *A&A*, 449, 1255

Biver N. et al., 2015, *Sci. Adv.*, 1, 1500863

Bockelée-Morvan D. et al., 2000, *A&A*, 353, 1101

Booth A. S., Ilee J. D., Walsh C., Kama M., Keyte L., van Dishoeck E. F., Nomura H., 2023b, *A&A*, 669, A53

Booth A. S., Law C. J., Temmink M., Leemker M., Macias E., 2023a, *A&A*, 678, A146

Booth A. S., van der Marel N., Leemker M., van Dishoeck E. F., Ohashi S., 2021, *A&A*, 651, L6

Booth A. S., Walsh C., Kama M., Loomis R. A., Maud L. T., Juhász A., 2018, *A&A*, 611, A16

Bosman A. D. et al., 2021, *ApJS*, 257, 7

Bruderer S., 2013, *A&A*, 559, A46

Bruderer S., van Dishoeck E. F., Doty S. D., Herczeg G. J., 2012, *A&A*, 541, A91

Calmonte U. et al., 2016, *MNRAS*, 462, S253

Charnley S. B., 1997, *MNRAS*, 291, 455

Chen Y. J. et al., 2015, *ApJ*, 798, 80

Cleeves L. I., Öberg K. I., Wilner D. J., Huang J., Loomis R. A., Andrews S. M., Guzman V. V., 2018, *ApJ*, 865, 155

Currie T., Cloutier R., Brittain S., Grady C., Burrows A., Muto T., Kenyon S. J., Kuchner M. J., 2015, *ApJ*, 814, L27

Dello Russo N., DiSanti M. A., Mumma M. J., Magee-Sauer K., Rettig T. W., 1998, *Icarus*, 135, 377

Dutrey A. et al., 2011, *A&A*, 535, A104

Endres C. P., Schlemmer S., Schilke P., Stutzki J., Müller H. S., 2016, *J. Mol. Spectrosc.*, 327, 95

Estrada P. R., Mosqueira I., Lissauer J. J., D'Angelo G., Cruikshank D. P., 2009, in Pappalardo R. T., McKinnon W. B., Khurana K. K., eds, *Europa*. Univ. Arizona Press, Tucson, p. 27

Fedele D., Toci C., Maud L. T., Lodato G., 2021, *A&A*, 651, A90

Ferrante R. F., Moore M. H., Spiliotis M. M., Hudson R. L., 2008, *ApJ*, 684, 1210

Foreman-Mackey D., Hogg D. W., Lang D., Goodman J., 2013, *PASP*, 125, 306

Fromang S., Terquem C., Balbus S. A., 2002, *MNRAS*, 329, 18

Fuente A. et al., 2017, *ApJ*, 851, L49

Furuya K., Hama T., Oba Y., Kouchi A., Watanabe N., Aikawa Y., 2022, *ApJ*, 933, L16

Gaia Collaboration, 2018, *A&A*, 616, A1

Galland N., Caralp F., Rayez M.-T., Hannachi Y., Loison J.-C., Dorthe G., Bergeat A., 2001, *J. Phys. Chem. A*, 105, 9893

Graedel T. E., Langer W. D., Frerking M. A., 1982, *ApJS*, 48, 321

Guilloteau S. et al., 2016, *A&A*, 592, A124

Guilloteau S., Di Folco E., Dutrey A., Simon M., Grosso N., Piétu V., 2013, *A&A*, 549, A92

Hobbs R., Shorttle O., Madhusudhan N., 2022, *MNRAS*, 516, 1032

Hueso R., Guillot T., 2003, *Space Sci. Rev.*, 106, 105

Jermyn A. S., Kama M., 2018, *MNRAS*, 476, 4418

Jiménez-Escobar A., Muñoz Caro G. M., 2011, *A&A*, 536, A91

Jiménez-Escobar A., Muñoz Caro G. M., Chen Y. J., 2014, *MNRAS*, 443, 343

Kama M. et al., 2016a, *A&A*, 588, A108

Kama M. et al., 2016b, *A&A*, 592, A83

Kama M., Shorttle O., Jermyn A. S., Folsom C. P., Furuya K., Bergin E. A., Walsh C., Keller L., 2019, *ApJ*, 885, 114

Keyte L. et al., 2023, *Nat. Astron.*, 7, 684

Lauretta D. S., Kremser D. T., Fegley Bruce J., 1996, *Icarus*, 122, 288

Law C. J., Booth A. S., Öberg K. I., 2023, *ApJ*, 952, L19

Le Gal R. et al., 2021, *ApJS*, 257, 12

Le Gal R., Öberg K. I., Loomis R. A., Pegues J., Bergner J. B., 2019, *ApJ*, 876, 72

Le Roy L. et al., 2015, *A&A*, 583, A1

Leconte J., Chabrier G., 2013, *Nat. Geosci.*, 6, 347

Liu S.-F., Hori Y., Müller S., Zheng X., Helled R., Lin D., Isella A., 2019, *Nature*, 572, 355

Loomis R. A., Öberg K. I., Andrews S. M., Walsh C., Czekala I., Huang J., Rosenfeld K. A., 2018, *AJ*, 155, 182

McClure M. K. et al., 2023, *Nat. Astron.*, 7, 431

McElroy D., Walsh C., Markwick A. J., Cordner M. A., Smith K., Millar T. J., 2013, *A&A*, 550, A36

McMullin J. P., Waters B., Schiebel D., Young W., Golap K., 2007, in Shaw R. A., Hill F., Bell D. J., eds, *ASP Conf. Ser. Vol. 376, Astronomical Data Analysis Software and Systems XVI*. Astron. Soc. Pac., Tucson, Arizona, p. 127

Meeus G. et al., 2012, *A&A*, 544, A78

Meeus G. et al., 2013, *A&A*, 559, A84

Miley J. M., Panić O., Haworth T. J., Pascucci I., Wyatt M., Clarke C., Richards A. M. S., Ratzka T., 2019, *MNRAS*, 485, 739

Miotello A. et al., 2019, *A&A*, 631, A69

Moll R., Garaud P., Mankovich C., Fortney J. J., 2017, *ApJ*, 849, 24

Müller H. S., Schlöder F., Stutzki J., Winnewisser G., 2005, *J. Mol. Spectrosc.*, 742, 215

Müller T. S., Roth D. A., Winnewisser G., 2001, *A&A*, 370, L49

Mumma M. J., Charnley S. B., 2011, *ARA&A*, 49, 471

Nettelmann N., Fortney J. J., Moore K., Mankovich C., 2015, *MNRAS*, 447, 3422

Nguyen T., Oba Y., Sameera W. M. C., Kouchi A., Watanabe N., 2021, *ApJ*, 922, 146

Oba Y., Tomaru T., Lamberts T., Kouchi A., Watanabe N., 2018, *Nat. Astron.*, 2, 228

Öberg K. I., Murray-Clay R., Bergin Edwin A. E.-M. K., 2011, *ApJ*, 743, L16

Öberg K. I., Wordsworth R., 2019, *AJ*, 158, 194

Pacetti E. et al., 2022, *ApJ*, 937, 36

Pasek M. A., Milsom J. A., Ciesla F. J., Lauretta D. S., Sharp C. M., Lunine J. I., 2005, *Icarus*, 175, 1

Pety J., 2018, in Submillimetre Single-dish Data Reduction and Array Combination Techniques. ESO, Garching, Germany, p. 11

Phuong N. T. et al., 2018, *A&A*, 616, L5

Pickles A. J., 1998, *PASP*, 110, 863

Pinilla P., Birnstiel T., Walsh C., 2015, *A&A*, 580, A105

Quanz S. P., Amara A., Meyer M. R., Girard J. H., Kenworthy M. A., Kasper M., 2015, *ApJ*, 807, 64

Rawlings J. M. C., 2022, *MNRAS*, 517, 3804

Rivièvre-Marichalar P. et al., 2021, *A&A*, 652, A46

Rivièvre-Marichalar P., Fuente A., Navarro-Almaida D., Baruteau C., 2023, in Proceedings of the XV Scientific Meeting of the Spanish Astronomical, La Laguna, Spain, p. 405

Santos J. C., Linnartz H., Chuang K.-J., 2023, *A&A*, 678, A112

Savage B. D., Sembach K. R., 1996, *ApJ*, 470, 893

Schöier F. L., van der Tak F. F. S., van Dishoeck E. F., Black J. H., 2005, *A&A*, 432, 369

Semenov D. et al., 2018, *A&A*, 617, A28

Sturm J. A. et al., 2023, *A&A*, 679, A138

Teague R. et al., 2016, *A&A*, 592, A49

Teague R., 2020

Thi W.-F. et al., 2011, *A&A*, 530, L2

Tieftrunk A., Pineau des Forets G., Schilke P., Walmsley C. M., 1994, *A&A*, 289, 579

Turri D. et al., 2021, *ApJ*, 909, 40

VanderPlas J. T. et al., 2018, *ApJS*, 236, L16

van Dishoeck E. F., Blake G. A., 1998, *A&A*, 36, 317

Wakelam V., Caselli P., Ceccarelli C., Herbst E., Castets A., 2004, *A&A*, 422, 159

Walsh C. et al., 2014, *ApJ*, 791, L6

Walsh C., Daley C., Facchini S., Juhász A., 2017, *A&A*, 607, A114

Wilson T. L., Rood R., 1994, *ARA&A*, 32, 191

Woodall J., Agúndez M., Markwick-Kemper A. J., Millar T. J., 2007, *A&A*, 466, 1197

Wright C. M. et al., 2015, *MNRAS*, 453, 414

Zhang K., Bergin E. A., Schwarz K., Krijt S., Ciesla F., 2019, *ApJ*, 883, 98

Zhang K., Bosman A. D., Bergin E. A., 2020, *ApJ*, 891, L16

## APPENDIX A: ALMA CONTINUUM OBSERVATION

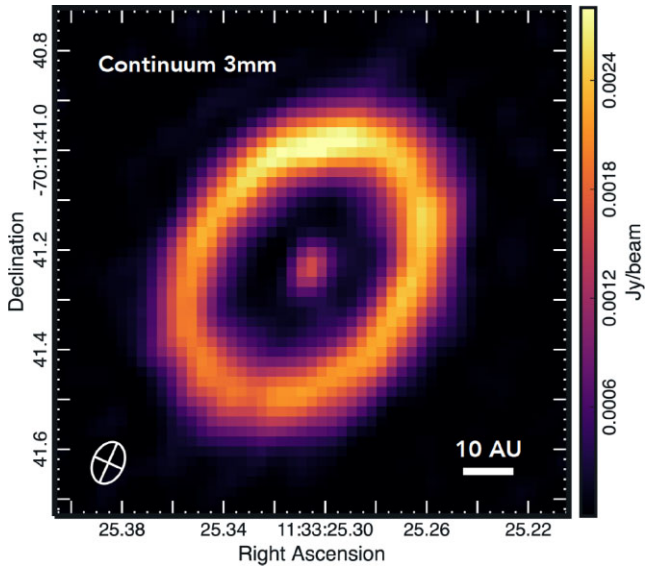


**Figure A1.** ALMA 3 mm continuum observation. The inner dust ring ( $r \sim 22-40$  au) is well-resolved, and the small inner dust disc is detected ( $r \sim 1$  au). Beam size indicated by the white ellipse in the lower left.

## APPENDIX B: DALI FIDUCIAL MODEL PARAMETERS AND UPDATES

We improve the fit to the dust continuum emission by simultaneously fitting 870  $\mu\text{m}$  continuum radial profile (Fedele et al. 2021) and 3 mm continuum radial profile (this work). We find that the combined data are best fit with a central cavity that extends to  $\sim 22$  au, compared to 13 au used in our previous study. We fit the ring-like structure of the outer disc by fully depleting the model of large dust grains between 40–150 au.

To ensure that the SED remains well fitted, we run a large grid of  $\sim 5000$  models using the updated dust structure. We vary the parameters  $r_{\text{gap}}$ ,  $\psi$ ,  $h_c$ ,  $\Delta_{g/d}$ ,  $\delta_{\text{dust}}$ ,  $\chi$ ,  $f$ , and  $\Sigma_c$ , finding that the new model is best fit by increasing the settling parameter  $f$  from 0.85 to 0.95, and the flaring index  $\psi$  from 0.20 to 0.25. The critical surface density,  $\Sigma_c$  is slightly increased from  $82.75 \text{ g cm}^{-2}$  to  $87.25 \text{ g cm}^{-2}$ , such that the total dust mass remains roughly the same as our original model, accounting for the mass removed by extending the cavity and introducing an outer dust gap. All other physical model parameters remain unchanged.

We explore the impact of altering the dust structure on the chemical abundances by running a grid of models in which [C/H] and [O/H] are varied between  $2 \times 10^{-6}$  and  $2 \times 10^{-4}$ . For each case, we consider variations in the level of gas depletion in the central cavity, ranging from  $\delta_{\text{gas}} = 10^{-5}$ –1. As done previously in Keyte et al. (2023), we fit to the CO ladder, a wide range of other disc-integrated line fluxes, and various spectral line and radial intensity profiles (see that work for a full list of the data). As before, we find that the model is best fit with a C/O ratio of 0.5, with [C/H] slightly increased from  $1 \times 10^{-5}$  to  $1.5 \times 10^{-5}$ , and [O/H] slightly increased from  $2 \times 10^{-5}$  to  $3 \times 10^{-5}$ . Gas within the central cavity is found to be severely depleted, with a best-fitting value of  $\delta_{\text{gas}} = 10^{-5}$ .

Fiducial model parameters are listed in Table B1 and initial atomic abundances are listed in Table B2.

**Table B1.** Fiducial HD 100546 disc model parameters.

Parameter	Description	Fiducial
$R_{\text{sub}}$	Sublimation radius	0.25 au
$R_{\text{gap}}$	Inner disc size	1.0 au
$R_{\text{cav}}$	Cavity radius	22 au
$R_{\text{out}}$	Disc outer radius	1000 au
$R_c$	Critical radius for surface density	50 au
$\delta_{\text{gas}}$	Gas depletion factor inside cavity	$10^{-5}$
$\delta_{\text{dust}}$	Dust depletion factor inside cavity	$10^{-4}$
$\gamma$	Power law index of surface density profile	1.0
$\chi$	Dust settling parameter	0.2
$f$	Large-to-small dust mixing parameter	0.95
$\Sigma_c$	$\Sigma_{\text{gas}}$ at $R_c$	$87.25 \text{ g cm}^{-2}$
$h_c$	Scale height at $R_c$	0.10
$\psi$	Power law index of scale height	0.25
$\Delta_{g/d}$	Gas-to-dust mass ratio	100
$L_*$	Stellar luminosity	$36 L_{\odot}$
$L_X$	Stellar X-ray luminosity	$7.94 \times 10^{28} \text{ ergs}^{-1}$
$T_X$	X-ray plasma temperature	$7.0 \times 10^7 \text{ K}$
$\zeta_{\text{cr}}$	Cosmic ray ionization rate	$3.0 \times 10^{-17} \text{ s}^{-1}$
$M_{\text{gas}}$	Disc gas mass	$9.89 \times 10^{-2} M_{\odot}$
$M_{\text{dust}}$	Disc dust mass	$1.06 \times 10^{-3} M_{\odot}$
$t_{\text{chem}}$	Time-scale for time-dependent chemistry	5 Myr

**Table B2.** Initial elemental abundances.

Species	$n_i/n_{\text{H}}$
H	1.0
He	$9.0 \times 10^{-2}$
C	$1.5 \times 10^{-5}$
N	$6.2 \times 10^{-5}$
O	$3.0 \times 10^{-5}$
S	$1.0 \times 10^{-8}$
Mg	$5.0 \times 10^{-7}$
Si	$5.0 \times 10^{-7}$
Fe	$5.0 \times 10^{-7}$

## APPENDIX C: ABUNDANCE MAPS

We present 2D abundance maps for 10 key molecular sulfur-bearing species extracted from our models. Fig. C1 shows abundance maps for sulfur-bearing species which contain carbon or oxygen, and Fig. C2 shows abundance maps for sulfur-bearing species containing neither carbon or oxygen. In each case, the left column shows abundances extracted from our model using a single initial sulfur abundance ( $S/\text{H} = 10^{-8}$ ) and the right column shows abundances extracted from the composite model. Fig. C3 shows abundances for all species in the ice-phase, extracted from the composite model.

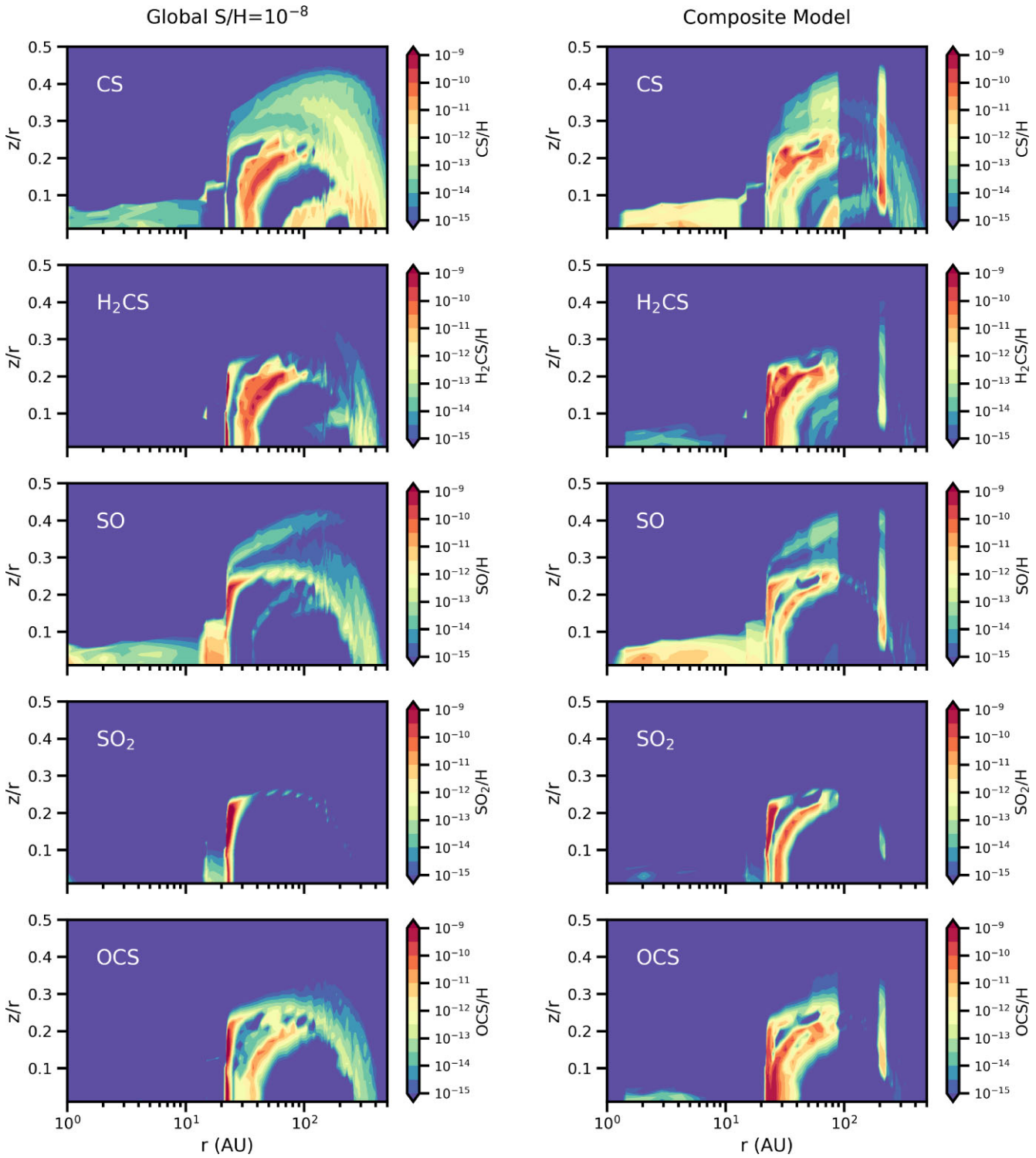


**Figure C1.** Abundance maps for the carbon- and oxygen-bearing sulfur species in models. *Left column:* model using a single sulfur abundance across the entire disc ( $S/H = 10^{-8}$ ). *Right column:* composite model using a radially varying sulfur abundance profile.

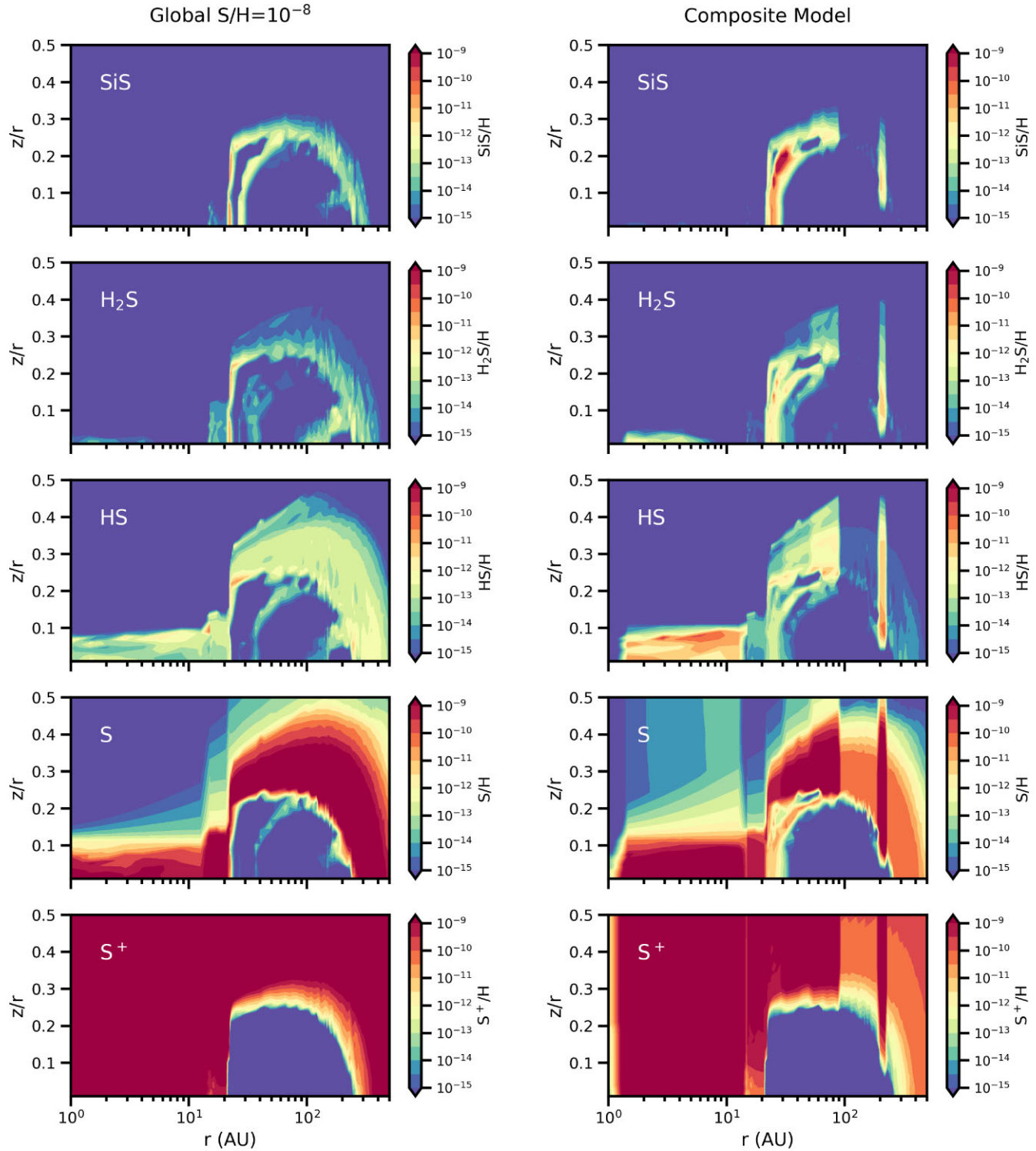


**Figure C2.** Abundance maps for the sulfur species containing no carbon or oxygen in our models. *Left column:* model using a single sulfur abundance across the entire disc ( $S/H = 10^{-8}$ ). *Right column:* composite model using a radially varying sulfur abundance profile.

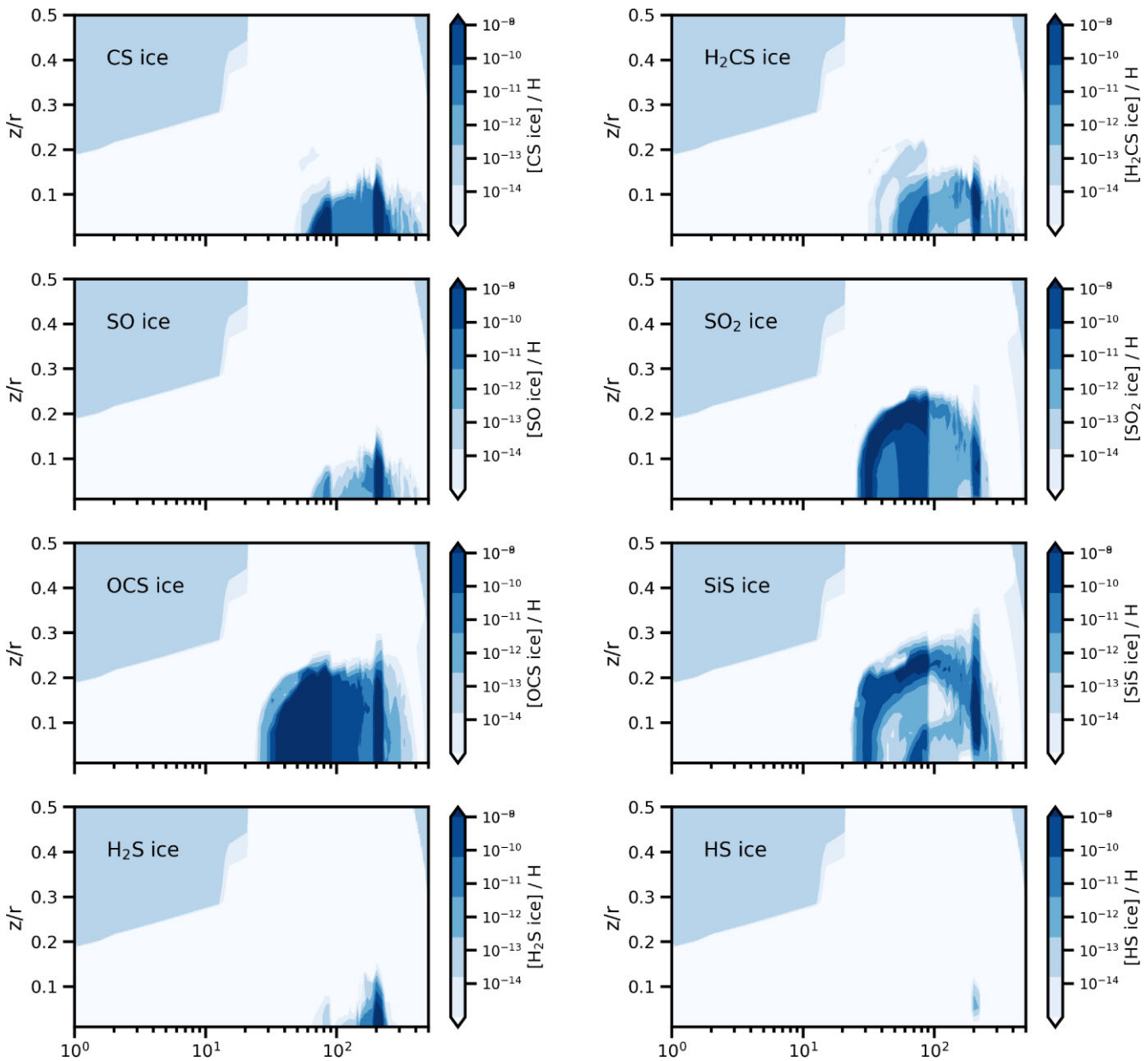


**Figure C3.** Abundance maps for sulfur-bearing ices in our composite model.

#### APPENDIX D: RADIAL INTENSITY PROFILE MCMC FITTING

Fig. D1 shows the posterior distribution for our MCMC fitting of the composite model. Fig. D2 shows the results from fitting our composite model to the region in which  $C/O = 1.5$ .

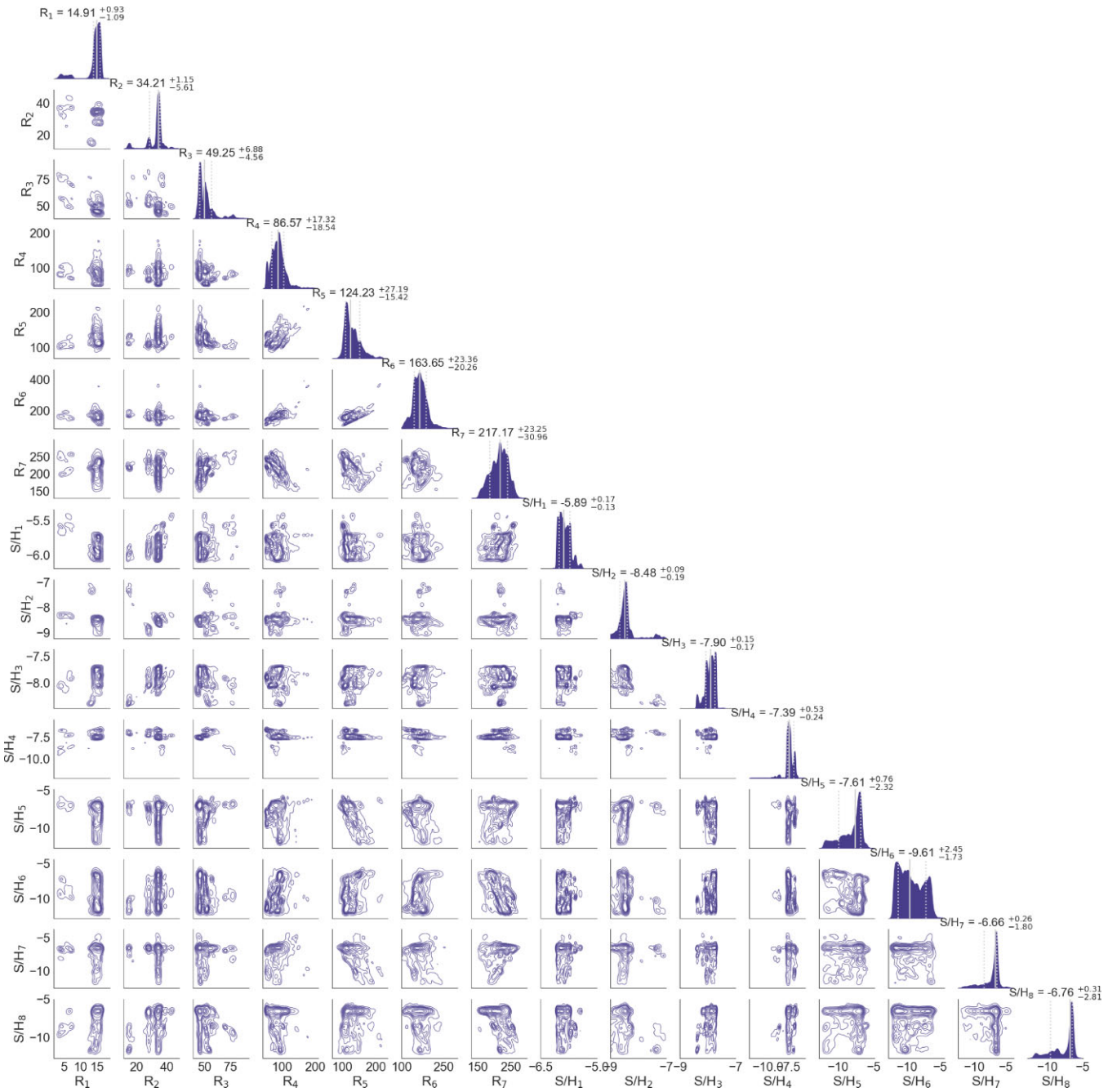


**Figure D1.** Posterior distribution for parameters used to simultaneously fit the SO  $7_7 - 6_6 + 7_8 - 6_7$  and CS 7–6 radial intensity profiles. Parameters labelled  $R_n$  are the radial locations where different models are spliced together (in au). Parameters labelled  $S/H_n$  are the  $\log_{10}$  sulfur abundances of the models fitted to each radial region.

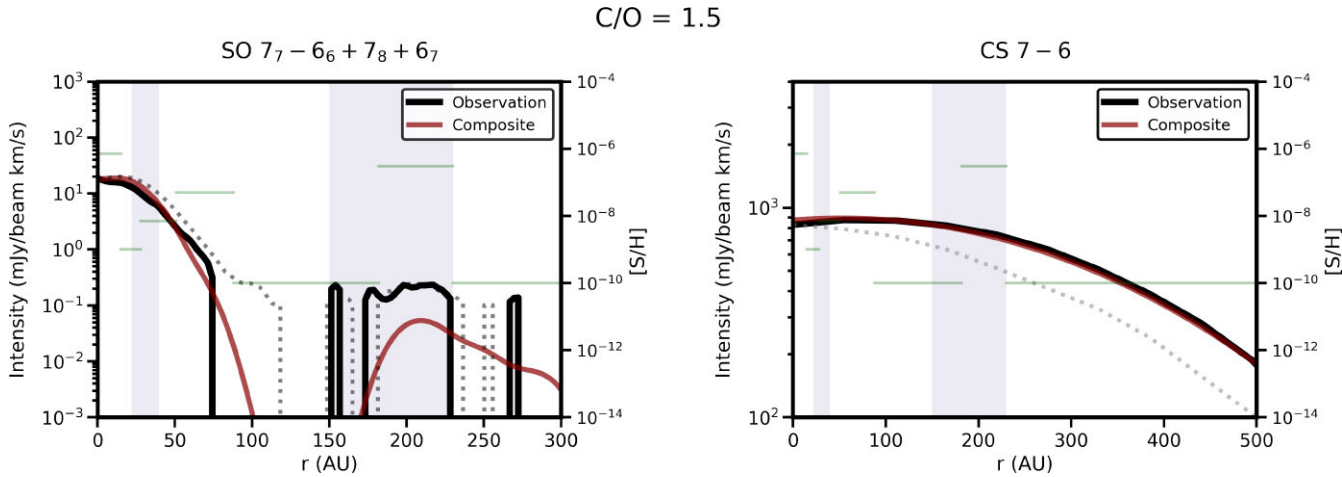


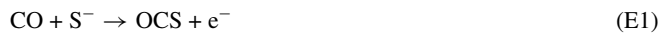
**Figure D2.** Radial intensity profiles extracted from deprojected integrated intensity maps, azimuthally averaged in the region of the disc where  $C/O = 1.5$ . Observations (black) and composite models (red). The models used in this region are initialized with abundances extracted from the  $C/O = 0.5$  model. Oxygen is then removed such that gas-phase  $C/O = 1.5$ , and the chemistry is evolved for 5 yr, following the procedure outlined in Keyte et al. (2023). Dotted grey lines show the observed radial intensity profiles in the region where  $C/O = 0.5$ , for comparison.

## APPENDIX E: COMPARISON WITH STARCHEM CHEMICAL MODELLING CODE

To assess the validity of the sulfur chemistry in our DALI models, we ran a set of comparison models using the STARCHEM chemical modelling code (Rawlings 2022, Rawlings, Keto & Caselli, submitted), which incorporates the full RATE12 data set (467 species and 5950 reactions; McElroy et al. 2013). Our goal was not to repeat the comprehensive modelling of the entire disc, but instead to perform a more in-depth examination of the chemistry, with a specific emphasis on validating the presence of OCS as a significant sulfur carrier in the gas phase. Such a comparison offers valuable insights into chemical network dependencies and potential consequences of omitting crucial species or reaction pathways from the DALI models.

To this end, we compared the chemistry at two vertical locations in the disc inside the inner dust ring at 22 au; the midplane ( $z/r = 0$ ) and disc atmosphere ( $z/r = 0.2$ ). These regions were selected as points at which the DALI model predicts OCS abundances to be relatively high in the gas phase ( $OCS/H \sim 10^{-9}$  in both locations). The inputs to STARCHEM were gas and dust densities/temperatures, cosmic ray and X-ray ionization rates, and the UV radiation field, each of which were taken from the relevant gridpoint locations in the DALI model. The chemistry was then initialized with elemental abundances following the DALI model (Table B2), and evolved for 5 Myr.

The outputs from STARCHEM broadly agree with our DALI model; we find OCS to be one of the major gas-phase sulfur carriers, with an abundance of  $OCS/H \sim 2 \times 10^{-10}$  at both locations. In the STARCHEM model, OCS formation is dominated by:



with some contribution from:



Our DALI model does not include  $S^-$ , and OCS is instead formed primarily by:



The main OCS destruction pathways in both models are cosmic ray and X-ray induced photodissociation and photoionization.

In addition to OCS, the STARCHEM model predicted the other major sulfur-carriers at this location to be  $H_2CS$  and  $SO_2$ . The STARCHEM  $H_2CS$  abundances of  $2.5 \times 10^{-10}$  ( $z/r = 0$ ) and  $2.0 \times 10^{-10}$  ( $z/r = 0.2$ ) are in agreement with the outputs of our DALI model within an order of magnitude. The  $SO_2$  abundances are slightly more divergent. The midplane abundance in the STARCHEM model is a factor of  $\sim 10$  higher than the DALI model, with formation facilitated via the route:



and



or



The higher  $SO_2$  abundance in the STARCHEM model is likely due to the lack of  $S_2$  in the DALI network, with  $SO_2$  formed pre-dominantly only through reactions (E8) and (E9) in the DALI model.

In the disc atmosphere, the  $SO_2$  abundance in the STARCHEM model falls off dramatically ( $SO_2/H = 8 \times 10^{-18}$ ), with  $S_2$  emerging as the main volatile sulfur carrier ( $S_2/H = 3 \times 10^{-9}$ ). A similar drop in the  $SO_2$  abundance is seen in the DALI model at a slightly higher vertical location ( $z/r \sim 0.25$ ). In both models, the main  $SO_2$  destruction pathways are once again cosmic ray and X-ray induced photodissociation and photoionization.

These findings offer valuable perspectives on sulfur chemistry, but it's important to acknowledge that there are likely to be important processes not captured in either model. For instance, although the

chemical network in the STARCHEM model is significantly more complex, it does not include gas–grain reactions, three-body reactions, and PAHs. The absence of gas–grain reactions could have significant ramifications for OCS-related chemistry, as laboratory experiments have demonstrated it is readily formed within icy grain mantles and can undergo significant processing (Ferrante et al.

2008; Nguyen et al. 2021). More work is needed to develop a deeper understanding of sulfur chemistry in planet-forming environments.

This paper has been typeset from a  $\text{\TeX}/\text{\LaTeX}$  file prepared by the author.